



HAL
open science

HARPS-N high spectral resolution observations of Cepheids II. The impact of the surface-brightness color relation on the Baade-Wesselink projection factor of η Aql

N. Nardetto, W. Gieren, J. Storm, V. Hocdé, G. Pietrzyński, P. Kervella, A. Mérand, A. Gallenne, D. Graczyk, B. Pilecki, et al.

► To cite this version:

N. Nardetto, W. Gieren, J. Storm, V. Hocdé, G. Pietrzyński, et al.. HARPS-N high spectral resolution observations of Cepheids II. The impact of the surface-brightness color relation on the Baade-Wesselink projection factor of η Aql. *Astronomy and Astrophysics - A&A*, 2023, 671, pp.A14. 10.1051/0004-6361/202245298 . hal-04310123

HAL Id: hal-04310123

<https://hal.science/hal-04310123v1>

Submitted on 1 Dec 2023

HAL is a multi-disciplinary open access archive for the deposit and dissemination of scientific research documents, whether they are published or not. The documents may come from teaching and research institutions in France or abroad, or from public or private research centers.

L'archive ouverte pluridisciplinaire **HAL**, est destinée au dépôt et à la diffusion de documents scientifiques de niveau recherche, publiés ou non, émanant des établissements d'enseignement et de recherche français ou étrangers, des laboratoires publics ou privés.



Distributed under a Creative Commons Attribution 4.0 International License

HARPS-N high spectral resolution observations of Cepheids

II. The impact of the surface-brightness color relation on the Baade-Wesselink projection factor of η Aql

N. Nardetto¹, W. Gieren^{2,3}, J. Storm⁴, V. Hlodčák⁵, G. Pietrzyński⁵, P. Kervella⁶, A. Mérand⁷, A. Gallenne^{2,8}, D. Graczyk⁵, B. Pilecki⁵, E. Poretti⁹, M. Rainer⁹, B. Zgirski⁵, P. Wielgórski⁵, G. Hajdu⁵, M. Górski⁵, P. Karczmarek², W. Narloch², and M. Taormina⁵

(Affiliations can be found after the references)

Received 26 October 2022 / Accepted 12 January 2023

ABSTRACT

Context. The Baade-Wesselink (BW) method of distance determination of Cepheids is used to calibrate the distance scale. Various versions of this method are mainly based on interferometry and/or the surface-brightness color relation (SBCR).

Aims. We quantify the impact of the SBCR, its slope, and its zero point on the projection factor. This quantity is used to convert the pulsation velocity into the radial velocity in the BW method. We also study the impact of extinction and of a potential circumstellar environment on the projection factor.

Methods. We analyzed HARPS-N spectra of η Aql to derive its radial velocity curve using different methods. We then applied the inverse BW method using various SBCRs in the literature in order to derive the BW projection factor.

Results. We find that the choice of the SBCR is critical: a scatter of about 8% is found in the projection factor for different SBCRs in the literature. The uncertainty on the coefficients of the SBCR affects the statistical precision of the projection factor only little (1–2%). Confirming previous studies, we find that the method with which the radial velocity curve is derived is also critical, with a potential difference on the projection factor of 9%. An increase of 0.1 in $E(B - V)$ translates into a decrease in the projection factor of 3%. A 0.1 mag effect of a circumstellar envelope (CSE) in the visible domain is rather small on the projection factor, about 1.5%. However, we find that a 0.1 mag infrared excess in the K band due to a CSE can increase the projection factor by about 6%.

Conclusions. The impact of the surface-brightness color relation on the BW projection factor is found to be critical. Efforts should be devoted in the future to improve the SBCR of Cepheids empirically, but also theoretically, taking their CSE into account as well.

Key words. stars: variables: Cepheids – stars: oscillations – stars: atmospheres – circumstellar matter – techniques: interferometric – techniques: spectroscopic

1. Introduction

The surface brightness color relation (SBCR) is a fundamental tool in modern astronomy. It is indeed used to easily and directly determine the angular diameter of any star from its photometric measurements, usually in two bands, in the visible and the near-infrared. The SBCRs are used, for instance, to derive the distances of eclipsing binaries in the Large Magellanic Cloud (Pietrzyński et al. 2013, 2019; Gallenne et al. 2018) and in the Small Magellanic Cloud (Graczyk et al. 2020) with exquisite precision. The reverse is also possible: if the parallax of a star (e.g., from the *Gaia* mission) is precise enough, the SBCR can be calibrated from eclipsing binaries in the Milky Way (Graczyk et al. 2021). The SBCRs are usually calibrated from interferometric observations, however (Di Benedetto 2005; Kervella et al. 2004d; Salsi et al. 2020a, 2021). Applying a homogeneous approach on a large number of interferometric data, these recent studies have shown that the SBCRs depend not only on the temperature of stars, but also on their luminosity class. This result was also confirmed from atmospheric models (Salsi et al. 2022). The SBCRs are also of high interest for the study of transiting exoplanet host stars. The radius of the planet can be directly derived from the radius of the star through the transit (Ligi et al. 2016). As an example, the SBCRs are currently implemented in the pipeline of the PLANetary Transits

and Oscillation of stars (PLATO) space mission, which provides an independent estimate of the stellar radius (Gent et al. 2022). The Stellar Parameters and Images with a Cophased Array (SPICA) interferometer installed at the Center for High Angular Resolution Astronomy (CHARA) will play an important role in this respect in the near future (Mourard et al. 2018, 2022; Pannetier et al. 2020).

Historically, the SBCRs are also used in the Baade-Wesselink (BW) method of Cepheid distance determination. Since their period-luminosity (PL) relation was established (Leavitt & Pickering 1912), Cepheid variable stars have been used to calibrate the distance scale (Hertzsprung 1913) and then the Hubble constant (Riess et al. 2011, 2016; Freedman et al. 2012). The BW method was first described by Lindemann (1918) and was later extended by Baade (1926) and Wesselink (1946). For almost a century, the BW method was used to derive the distance of Cepheids. The concept is simple: distances are computed using measurements of the angular diameter over the whole pulsation period along with the stellar radius variations deduced from the integration of the pulsation velocity V_{puls} . The latter is linked to the observed radial velocity (RV) by the projection factor $p = V_{\text{puls}}/\text{RV}$ (Hindsley & Bell 1986; Nardetto et al. 2004, 2009). The three basic versions of the BW method correspond to different ways of determining the angular diameter curve: the photometric version based on the

SBCRs (Fouque & Gieren 1997; Fouqué et al. 2007; Storm et al. 2011a,b), the interferometric version (Lane et al. 2000; Kervella et al. 2004c; Mérand et al. 2005), and the more recent version that combines several photometric bands, velocimetry, and interferometry (SPIPS; Mérand et al. 2015). Recently, a study has shown that the projection factors of Cepheids are highly dispersed (even for Cepheids with the same period), which limits the precision of the BW method to 5–10% (Trahin et al. 2021).

For the long-period Cepheid ℓ Car, the angular diameter curves derived from the infrared surface brightness relation and infrared interferometry, respectively, are consistent (Kervella et al. 2004b), while this is not the case for the short-period Cepheid δ Cep (Ngeow et al. 2012). In the SPIPS approach, Mérand et al. (2015) have resolved this discrepancy by adding an ad hoc infrared excess, which can be justified by the presence of a circumstellar environment (CSE) around Cepheids. The CSE of Cepheids was discovered by interferometry (Kervella et al. 2006; Mérand et al. 2006, 2007; Gallenne et al. 2013; Hocdé et al. 2021). Interestingly, a resolved structure around δ Cep was discovered in the visible spectral range using interferometry (Nardetto et al. 2016). Recently, Hocdé et al. (2020b) showed that the infrared excess of the Cepheids can be explained by a shell of ionized gas, whereas the favored hypothesis until now was dust. At the same time, Hocdé et al. (2020a) also showed that the ionization of the gas could come from shocks propagating in the chromosphere of the Cepheids. It appears from these studies that the CSE, like the projection factor, might bias the BW distance.

We secured spectroscopic observations with the High Accuracy Radial velocity Planet Searcher for the Northern hemisphere (HARPS-N) of the short period Cepheids δ Cep and η Aql. Nardetto et al. (2017) analyzed the projection factor of δ Cep. In this study, we focus on the SBCR issue. The overall goal is to clarify the impact of the SBCR on the BW projection factor. Indeed, many SBCRs are described in the literature, but their coefficients differ significantly (Salsi et al. 2020a). We start in Sect. 2 with the presentation of the HARPS-N data of η Aql, from which we derive a radial velocity curve as well as the atmospheric velocity gradient. Then, we collect photometric data (Sect. 3) and combine them with the SBCRs available in the literature (Sect. 4) in order to apply the inverse BW method and derive the projection factors (Sect. 6). We then further explore the impact of various parameters on the projection factor: zero point and slope of the SBCR, $E(B - V)$, and a possible CSE (Sect. 7). We conclude in Sect. 8. This paper is part of the international Araucaria Project, whose purpose is to provide an improved local calibration of the extragalactic distance scale out to distances of a few megaparsecs (Gieren et al. 2005).

2. HARPS-N spectroscopic observations

HARPS-N is a high-precision radial-velocity spectrograph installed at the Italian Telescopio Nazionale Galileo (TNG), which is a 3.58-meter telescope located at the Roque de los Muchachos Observatory on the island of La Palma, Canary Islands, Spain (Cosentino et al. 2012). HARPS-N is the northern hemisphere counterpart of the similar HARPS instrument installed at the ESO 3.6 m telescope at La Silla Observatory in Chile. The instrument covers the wavelength range from 3800 to 6900 Angstrom with a resolving power of $R \approx 115\,000$. A total of 98 spectra were secured between 27 March and 8 September 2015 in the framework of the OPTICON proposal 2015B/015. In order to calculate the pulsation phase of each spectrum, we used the recent ephemeris $P = 7.1765470$ d,

$T_0 = 2\,411\,998.2930$ d, and $\frac{dP}{dt} = 0.00000295060$ days yr⁻¹ from Csörnyei et al. (2022). The data are spread over 13 of the 23 pulsation cycles that elapsed between the first and last epoch. The final products of the HARPS-N data reduction software (DRS) installed at TNG (online mode) are background-subtracted, cosmic-corrected, flat-fielded, and wavelength-calibrated spectra (with and without merging of the spectral orders).

The DRS computes the cross-correlation function (noted ‘cc’ in the following) using a mask including thousands of lines covering the whole HARPS-N spectral ranges. The observer can select the mask among the masks that are available online, and the G2V mask was the closest to the η Aql spectral type (F6I). As a further step, we recomputed the cross-correlation function by using the HARPS-N DRS in the offline mode on the Yabi platform, considering a custom mask for a F6I star. Yabi (Hunter et al. 2012) is a Python web application installed at IA2¹ in Trieste that allows authorized users to run the HARPS-N DRS pipeline on their own proprietary data with custom input parameters. Figure 1 shows that the mean profiles reflect the large-amplitude radial pulsation. Then, the DRS computes the stellar radial velocity by fitting a Gaussian to the cross-correlation functions (RV_{cc-g}). However, Nardetto et al. (2006) have shown that the centroid velocity, that is, the first moment (or centroid) of the spectral line profile, is estimated as

$$RV_c = \frac{c}{\lambda_0} \frac{\int_{\text{line}} (\lambda - \lambda_0) S(\lambda) d\lambda}{\int_{\text{line}} S(\lambda) d\lambda}, \quad (1)$$

where $S(\lambda)$ is the observed line profile, c is the velocity of light, and λ_0 is the rest wavelength of the spectral line. This definition, at least on single lines, is most frequently adapted in the context of the BW method because this velocity is independent of stellar rotation or spectral line width variation. By applying the first moment to the cross-correlation function, we can derive the RV_{cc-c} velocity.

2.1. Cross-correlated radial velocity curves

We obtained four RV curves: RV_{cc-g} and RV_{cc-c} , combined with masks for spectral types G2V and F6I. We find no difference between G2 and F6I templates. We decided to keep the F6 template in the following. Tables A.1 and A.2 list the RV_{cc-g} and RV_{cc-c} values obtained with the custom F6I mask, respectively, while the data and the Fourier-interpolated radial velocity curves are shown in the top panel of Fig. 2. Measurements and interpolated curves in the figure were corrected from a γ -velocity of 14.87 km s⁻¹ corresponding to the average of the interpolated radial velocity curve RV_{cc-c} (F6 mask). In the bottom panel of Fig. 2, we overplot the RV_{cc-g} and RV_{cc-c} interpolated curves of HARPS-N with previous measurements found in the literature (Storm et al. 2011a; Borgniet et al. 2019; Kiss 1998; Barnes et al. 2005). The agreement between RV_{cc-g} and previous measurements (obtained with the same method) is good.

We find no evidence for cycle-to-cycle differences in the RV amplitude as exhibited by long-period Cepheids (Anderson 2014; Anderson et al. 2016). We find a significant difference between the RV_{cc-g} and RV_{cc-c} curves in terms of amplitude. The impact of this difference on the projection factor is discussed in Sect. 7.

2.2. Atmospheric velocity gradient

In this section, we apply the same approach as was presented in Nardetto et al. (2017). In brief, we considered the 17 unblended

¹ <https://www.ia2.inaf.it>

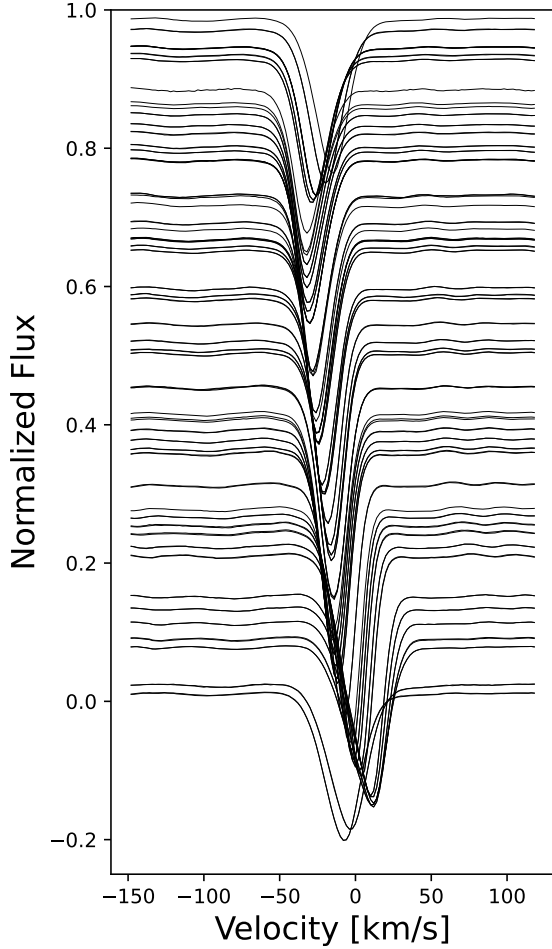


Fig. 1. Cross-correlated spectral line profile (using a template for an F6 star) as a function of the pulsation phase (indicated on the left of the diagram).

spectral lines presented in Table 1. For each of these lines, we derived the centroid velocity (RV_c) as defined previously (Eq. (1)). The radial velocity measurements associated with the spectral lines are presented in Fig. 3. The plotted RV_c curves were corrected for the γ -velocity value corresponding to the RV_{cc-c} curve. The residuals, that is, the γ -velocity offsets, between the curves are related to the line asymmetry and the k -term value (see Nardetto et al. 2008 for Cepheids and Nardetto et al. 2013, 2014 for other types of pulsating stars). Nardetto et al. (2007) split the projection factor into three quantities: $p = p_0 f_{\text{grad}} f_{o-g}$, where p_0 is the geometrical projection factor (linked to the limb darkening of the star); f_{grad} , which is a cycle-integrated quantity linked to the velocity gradient in the atmosphere of the star (i.e., between the considered line-forming region and the photosphere); and f_{o-g} , which is the relative motion of the optical pulsating photosphere with respect to the corresponding mass elements.

We derived f_{grad} associated with line i directly from HARPS-N observations using

$$f_{\text{grad}}(i) = \frac{b_0}{\Delta RV_c(i)}, \quad (2)$$

where

$$\Delta RV_c(i) = a_0 D(i) + b_0, \quad (3)$$

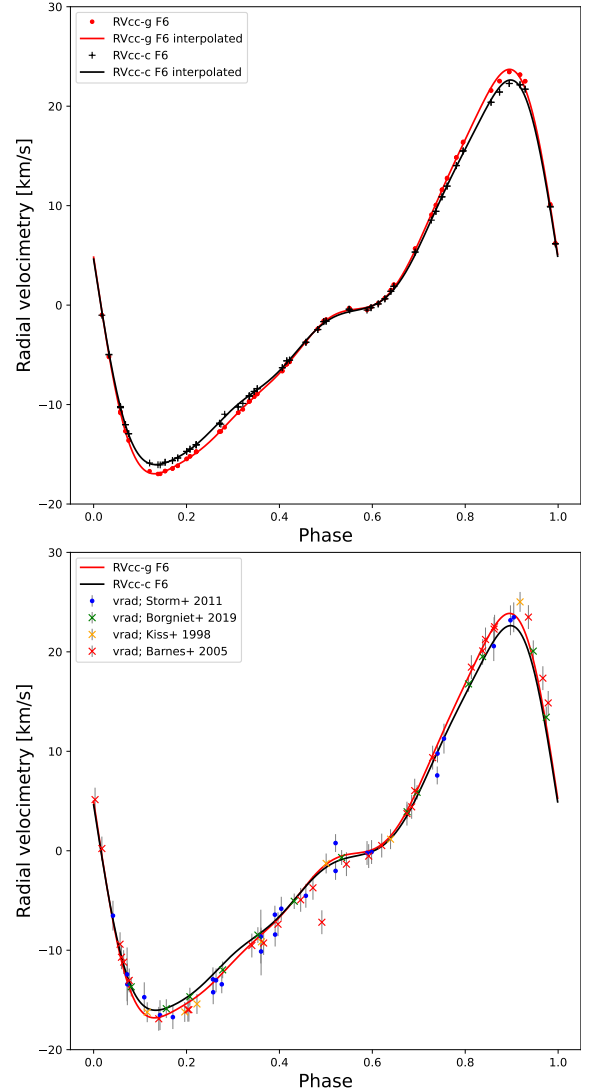


Fig. 2. Radial velocity curves of η Aql. Top: HARPS-N cross-correlated measurements (F6 template) using the Gaussian fit (RV_{cc-g} , red points) and the centroid (RV_{cc-c} , black points) methods to measure the velocity together with the corresponding Fourier-interpolated curves. Bottom: HARPS-N interpolated curves are shown together with the RV_{cc-g} measurements in the literature.

with $\Delta RV_c(i)$ the amplitude of the radial velocity curves associated with line i and $D(i)$, the line depth at minimum radius. In this definition, b_0 is the amplitude of the radial velocity associated with the photosphere of the star. By integrating RV_{cc-c} , we find that the phase corresponding to the minimum radius is $\phi = 0.015$. In the left panel of Fig. 4, we plot the line depth as a function of the pulsation phase associated with each of the 17 lines, as well as the depth of the cross-correlated profile. The RV_c and the line depth curves associated with each line were then interpolated using a Fourier analysis. In the right panel of Fig. 4, ΔRV_c is plotted as a function of D for each individual line. The values obtained for the RV_{cc-g} and RV_{cc-c} curves are also shown for comparison, as well as the whole range of the associated line depth over the cycle. We fit a linear trend to the data. We find

$$\Delta RV_c = [1.7 \pm 1.9]D + [37.4 \pm 0.5]. \quad (4)$$

The reduced χ^2 is 0.48. When a quadratic curve was fit to include line 2 (dash-dotted line) or excluded line 2 (dotted line),

Table 1. Spectral lines with their wavelength of reference λ_0 , excitation potential (Ep), and oscillator strengths $\log(gf)$.

Number	line	λ_0	Ep	$\log(gf)$
1	Fe I	4683.560	2.831	-2.319
2	Fe I	4896.439	3.883	-2.050
3	Ni I	5082.339	3.658	-0.540
4	Fe I	5367.467	4.415	0.443
5	Fe I	5373.709	4.473	-0.860
6	Fe I	5383.369	4.312	0.645
7	Ti II	5418.751	1.582	-2.110
8	Fe I	5576.089	3.430	-1.000
9	Fe I	5862.353	4.549	-0.058
10	Fe I	6003.012	3.881	-1.120
11	Fe I	6024.058	4.548	-0.120
12	Fe I	6027.051	4.076	-1.089
13	Fe I	6056.005	4.733	-0.460
14	Si I	6155.134	5.619	-0.400
15	Fe I	6252.555	2.404	-1.687
16	Fe I	6265.134	2.176	-2.550
17	Fe I	6336.824	3.686	-0.856

\AA
eV

we obtained a reduced χ^2 of 0.50 and 0.43, respectively. In any case, the results are consistent with a null atmospheric velocity gradient for η Aql ($\Delta RV_c = 37.89 \pm 0.23$, with a reduced χ^2 of 0.49). However, the differences in the velocity amplitudes found for the 17 lines are large enough to affect the projection significantly, as discussed in Sect. 7.

3. Photometric data

In order to apply the SBCR, we need photometry in the visual and in the infrared domains. For the visual photometry, we used data from Moffett & Barnes (1984), Berdnikov (2008), Barnes et al. (1997), Szabados (1977) and Kiss (1998), while for infrared photometry, we considered Welch & Evans (1984) and Barnes et al. (1997). The curves were interpolated using a Fourier analysis, and they are plotted in Fig. 5. The visual photometric data are in the Johnson system, while the infrared data are in the Cerro Tololo Inter-American Observatory (CTIO) system (Elias et al. 1982).

4. Comparison of the surface brightness color relations

As already shown previously (di Benedetto 1993), but using a method based on various selection criteria, Salsi et al. (2020a, 2021) have again confirmed the result that the SBCR depends on the stellar class, that is, on the stellar surface gravity. The difference is significant between dwarfs and giants, but it remains unclear between luminosity classes III, II, and I. Thus, when the SBCR version of the BW method is to be applied to Cepheids, it is important to consider an SBCR that is suitable for Cepheids. In Tables 2 and 3 we list the linear and nonlinear SBCRs from the literature that might be applicable to Cepheids, respectively. Some of the SBCRs are specific to Cepheids, that is, they are based on observations of Cepheids (indicated by ‘‘Cep’’ in Tables 2 and 3), while others are typically for stellar classes III, II, or I. Some of the SBCRs were considered as valid for all

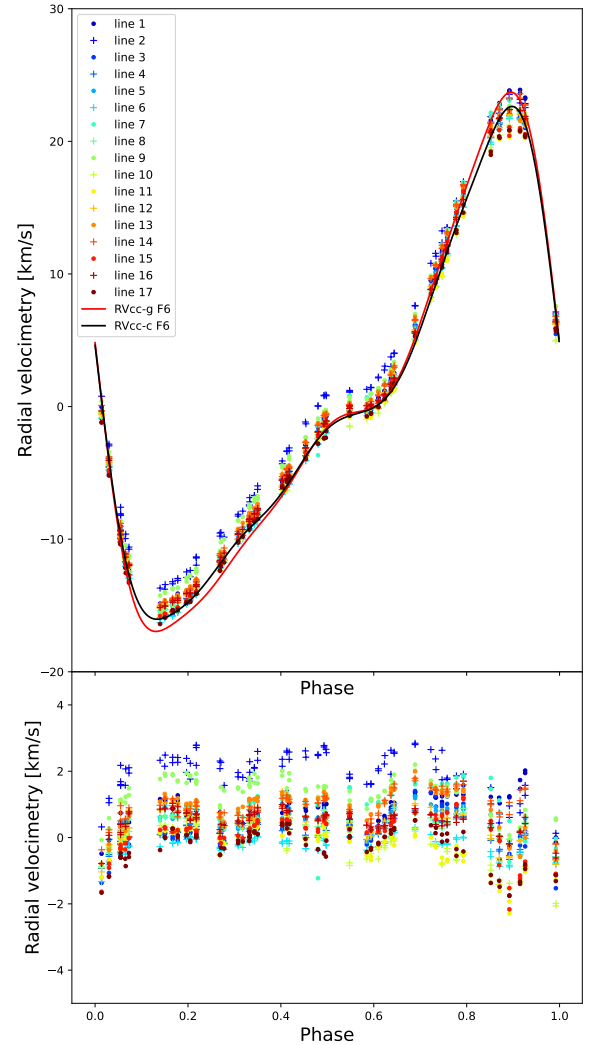


Fig. 3. Radial velocity curves of η Aql for different spectral lines. Top: HARPS-N interpolated curves are shown together with the radial velocity derived using the centroid method RV_{cc-c} for the 17 unblended spectral lines listed in Table 1. Bottom: difference compared to the RV_{cc-c} curve.

classes by their authors. They are indicated by ‘‘all’’ in the tables. The photometric systems used to calibrate the linear and nonlinear SBCRs are provided in Table 4. The systems used are the Johnson system (Johnson et al. 1966), the CTIO system (Elias et al. 1982), the South African Astronomical Observatory (SAAO) system (Carter 1990), and the Two-Micron Sky Survey (TMSS) system, also called InfraRed Caltech catalog (IRC; Neugebauer & Leighton 1969). In the visual domain, the generally used photometric system is the Johnson system, except for K04, who used the Cousins system. The vB99 SBCR used the Catalog of Infrared Observations (CIO) from Gezari et al. (1993) for the infrared data and the General Catalog of Photometric Data (GCPD) for the visual magnitudes (Mermilliod et al. 1997). These two catalogs provide a compilation of infrared and visual data in various photometric systems, respectively. The impact of these systems on the projection factor is discussed in Sect. 7.

In the upper panel of Fig. 6, we plot the 19 SBCRs of Tables 2 and 3. In the lower panel, we plot the difference between these SBCRs and the fiducial SBCR of (Kervella et al. 2004a; K04). In this second panel, we plot only the SBCRs whose validity domain is consistent with the $V - K$ color range of η Aql (i.e.,

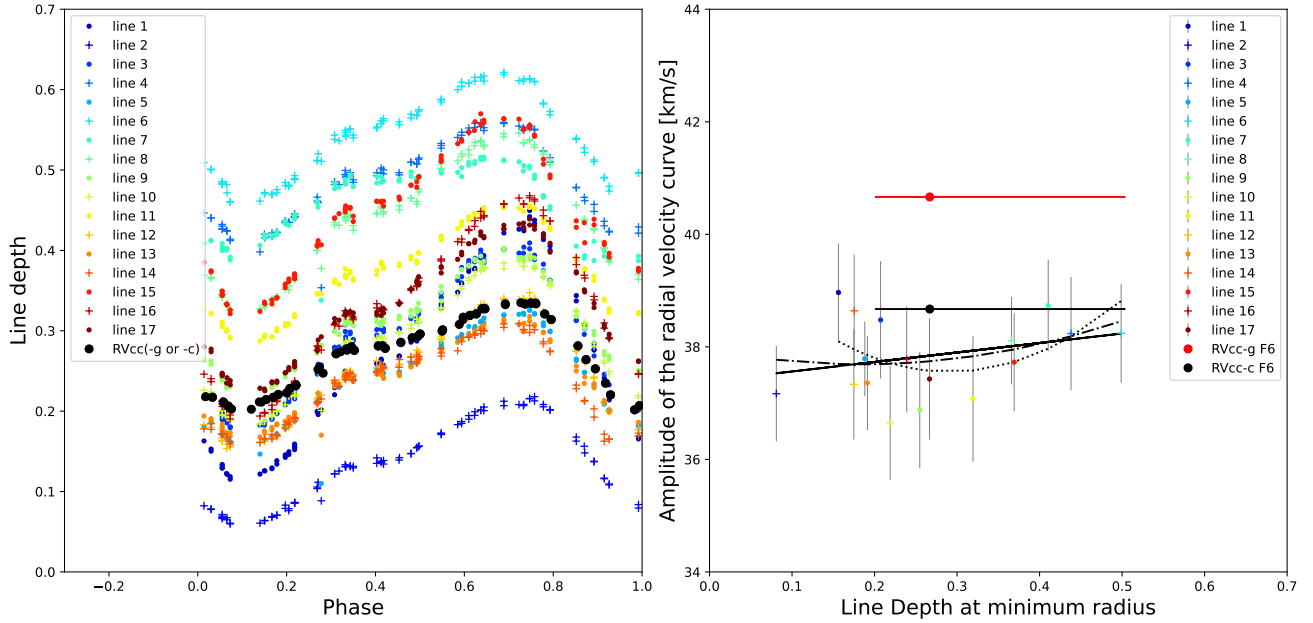


Fig. 4. Measure of the atmospheric velocity gradient of η Aql. Left: depth for the 17 spectral lines as a function of the pulsation phase, as well as the depth of the cross-correlated profile (black dots). The quantity corresponding to the line depth is slightly different for the Gaussian fit (RV_{cc-g}) method or the centroid (RV_{cc-c}), but it provides the same values. Right: amplitude of the radial velocity curves of the 17 spectral lines listed in Table 1, plotted vs. the line depth, at minimum radius. The amplitudes of the RV_{cc-g} and RV_{cc-c} curves (template F6) are shown for comparison (red and black dots, respectively) together with the minimum and maximum depth of the cross-correlated profile (horizontal red and black lines). Different fits are processed (see the text for the explanation).

Table 2. All the linear SBCRs found in the literature that are applicable to Cepheids.

Ref	Class	l_1	l_2	N	b	σ_b	a	σ_a	σ_{rms}
dB93	III	1.4	3.7	8	3.9270	0.0000	-0.1220	0.0000	0.0030
dB93	I, II	0.5	4.3	6	3.9540	0.0000	-0.1330	0.0000	0.0070
dB93	I, II	0.5	4.3	6	3.9580	0.0000	-0.1390	0.0000	0.0070
F97	III	2.22	4.11	10	3.9300	0.0120	-0.1240	0.0040	0.0080
F97	I, II	0.52	5.53	13	3.9140	0.0230	-0.1190	0.0070	0.0320
F97	Cep	0.8	2.4	10	3.9470	0.0000	-0.1310	0.0000	0.0000
N02	III	0.7	4	57	3.9340	0.0050	-0.1230	0.0020	0.0110
N02	Cep	0.7	4	59	3.9560	0.0110	-0.1340	0.0050	0.0260
K04	Cep	1.1	2.4	9	3.9530	0.0006	-0.1336	0.0008	0.0150
vB99	I, II, III	2	8	163	3.8862	0.0260	-0.1115	0.0050	0.0235
G04	III	1.6	3.9	74	3.9287	0.0070	-0.1225	0.0025	0.0023
G04	I, II	-0.85	4.1	21	3.9172	0.0095	-0.1215	0.0040	0.0024
P19	III	2.07	2.71	41	3.9537	0.0017	-0.1330	0.0017	0.0018
S21	II, III	1.8	3.8	70	3.9278	0.0016	-0.1220	0.0006	0.0022
		mag	mag		mag	mag			mag

Notes. These SBCRs are provided using the same formalism: $F_{V_0} = a(V - K)_0 + b$. $l_1 = (V - K)_1$ and $l_2 = (V - K)_2$ are the limit of the validity domain of the SBCRs. The references are the following: dB93 (di Benedetto 1993), F97 (Fouque & Gieren 1997), N02 (Nordgren et al. 2002), K04 (Kervella et al. 2004a), vB99 (van Belle 1999), G04 (Groenewegen 2004), P19 (Pietrzyński et al. 2013), S21 (Salsi et al. 2021). See Appendix F of Nardetto (2018) for more details about these SBCRs. The second, third, and fourth columns provide the validity domain in terms of class and $(V - K)_0$ color. Only SBCRs dB93 (III) and dB93 (I, II) are not corrected for extinction (we kept them for comparison). N is the number of measurements over which the calibration was performed. b and a are the coefficients of the SBCR in the form $F_{V_0} = a(V - K)_0 + b$. The statistical uncertainty on the coefficients of the SBCR is also provided, as is the rms. The SBCRs are based on various definitions in the literature. Some transformations were necessary to derive the coefficients of the SBCRs, their uncertainties, and the rms.

from about 1.1 to 1.8 mag). We use the SBCR of K04 as a reference as it is often used in the literature when the BW method is used. As an indication, the rms of the K04 relation is shown in the upper panel of the figure as a gray zone. The rms of the other SBCRs can be found in Tables 2 and 3. The agreement between the 19 SBCRs is better than about 0.0075 mag between

1.5 and 2.5 mag in $V - K$. Outside this range, significant disagreements are found. In Fig. 7 we plot the slope of the linear SBCRs as a function of the zero point, with the associated statistical uncertainties when available. The relations disagree clearly, but these disagreements come in a large part from the fact that the slope and zero point of the SBCRs are correlated. This is

Table 3. Coefficients a_k for polynomial SBCRs in the form $S_{V_0} = \sum_{k=0}^k a_k(V - K)_0^k$ with their corresponding uncertainty σ_{a_k} .

Ref	Class	l_1	l_2	$a_0 \pm \sigma_{a_0}$	$a_1 \pm \sigma_{a_1}$	$a_2 \pm \sigma_{a_2}$	$a_3 \pm \sigma_{a_3}$	$a_4 \pm \sigma_{a_4}$	$a_5 \pm \sigma_{a_5}$	rms
dB98	III	1.5	3.7	2.657	1.421	-0.033				0.03
C14	all	-0.9	3.7	$2.624_{\pm 0.009}$	$1.798_{\pm 0.020}$	$-0.776_{\pm 0.034}$	$0.517_{\pm 0.036}$	$-0.150_{\pm 0.015}$	$0.015_{\pm 0.002}$	0.10
C14	I+II	-0.88	3.21	2.291	2.151	-0.461	0.073			0.08
C14	III	-0.74	3.69	2.497	1.916	-0.335	0.050			0.07
dB05	all	-0.1	3.7	$2.565_{\pm 0.016}$	$1.483_{\pm 0.015}$	$-0.044_{\pm 0.005}$				0.04

Notes. $l_1 = (V - K)_1$ and $l_2 = (V - K)_2$ are the limit of the validity domain of the SBCRs. The number of measurements N over which the calibrations of the five SBCRs listed in this table were performed are 14, 132, 12, 41, and 41. The rms of this table (based on the S_{V_0} definition of the surface brightness) should be divided by 10 (following Eq. (8)) to be compared to the rms of Table 2, which is based on the F_{V_0} definition of the SBCR. The references are the following: dB98 (di Benedetto 1998, Eq. (3)), C14 (Challouf et al. 2014), dB05 (Di Benedetto 2005).

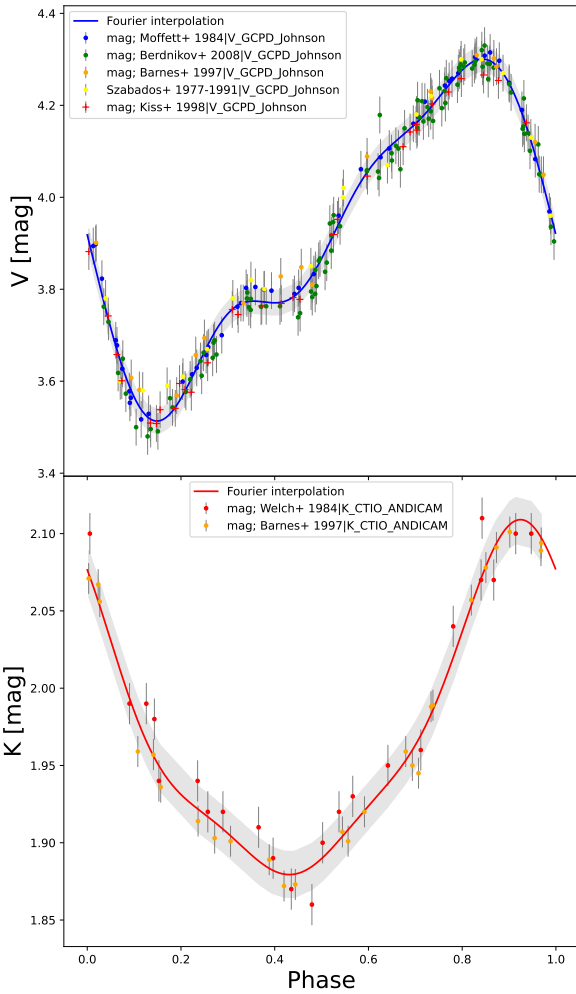


Fig. 5. Photometric curves of η Aql. Top: V -band photometric measurements from the literature plotted against the pulsation phase. The solid blue line is an interpolation using a Fourier series. Bottom: same as in the top panel, but in the K -band. The gray zones correspond to the uncertainty in the fit.

because the barycenter of the measurements is usually not taken as a reference to calculate the zero point.

5. Comparison of the angular diameter curves

In this section, we apply the SBCRs in order to derive the angular diameter curves. To do this, we used the method described

Table 4. Infrared photometric systems used to calibrate the linear and nonlinear SBCRs indicated in Tables 2 and 3, respectively.

Ref	Class	Photometric systems
dB93	III	Johnson
dB93	I, II	Johnson
dB93	I, II	Johnson
F97	III	Johnson
F97	I, II	Johnson
F97	Cep	Johnson
N02	III	Johnson
N02	Cep	Johnson + CTIO
K04	Cep	SAAO
vB99	I, II, III	Various
G04	III	Johnson + IRC
G04	I, II	Johnson + IRC
P19	III	SAAO
S21	II, III	Johnson + IRC + SAAO
dB98	III	Johnson
C14	all	Johnson
C14	I+II	Johnson
C14	III	Johnson
dB05	all	Johnson

in Fouque & Gieren (1997), Fouqué et al. (2007), Storm et al. (2011a,b), which relies on the following relation:

$$\log \theta_{LD}(\phi_i) = 8.4414 - 0.2V_0(\phi_i) - 2F_{V_0}(\phi_i). \quad (5)$$

where θ_{LD} , V , and F_V are the limb-darkened angular diameter, the magnitude, and the surface brightness, respectively, in the V band at the corresponding phase of pulsation ϕ_i . The SBCRs as listed in Table 2 are defined by

$$F_{V_0} = a(V - K)_0 + b, \quad (6)$$

where K is the magnitude in the K band. The subscript 0 refers to the magnitudes corrected for interstellar extinction. By definition, the interstellar absorption A_V in the visible band is given by $A_V = R_V \times E(B - V)$, where $E(B - V)$ is the $B - V$ color excess, and R_V is the total-to-selective absorption in the V band. The nonlinear SBCRs in the literature (Table 3) are most often

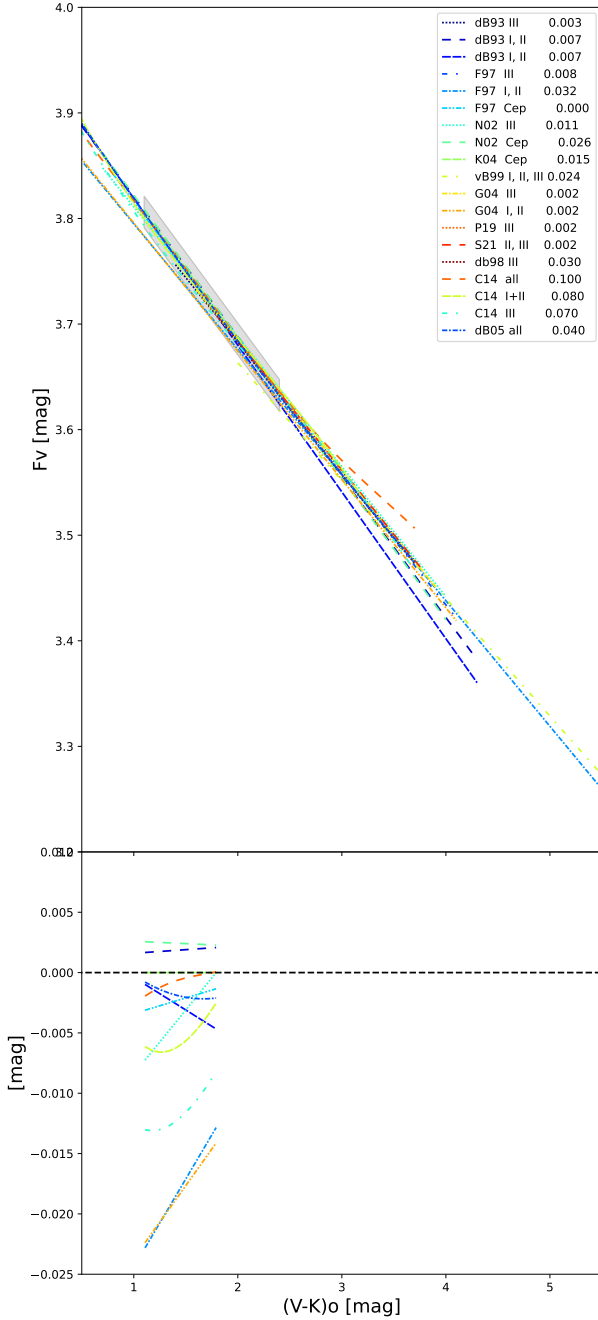


Fig. 6. SBCRs in the literature that are consistent with an application to Cepheids. Top: SBCR in the literature plotted over the $(V - K)_0$ validity domain. The gray zone correspond to the rms of K04 SBCR, i.e., 0.015 mag. The rms of other SBCRs (in mag) is indicated in the legend. Bottom: SBCRs compared to K04 in the $(V - K)_0$ range corresponding to η Aql pulsation. SBCRs that are partly or not at all consistent with the $(V - K)_0$ range of η Aql (see Table 5) are not indicated in this second panel.

provided in the form

$$S_{V_0} = \sum_{k=0}^k a_k (V - K)_0^k. \quad (7)$$

When $M_{\text{bol}\odot} = 4.74$ mag and $f_{\odot} = 1361$ W/m² (Prša et al. 2016) are used, the conversion into F_V is by definition

$$F_V = 4.2196 - 0.1S_V. \quad (8)$$

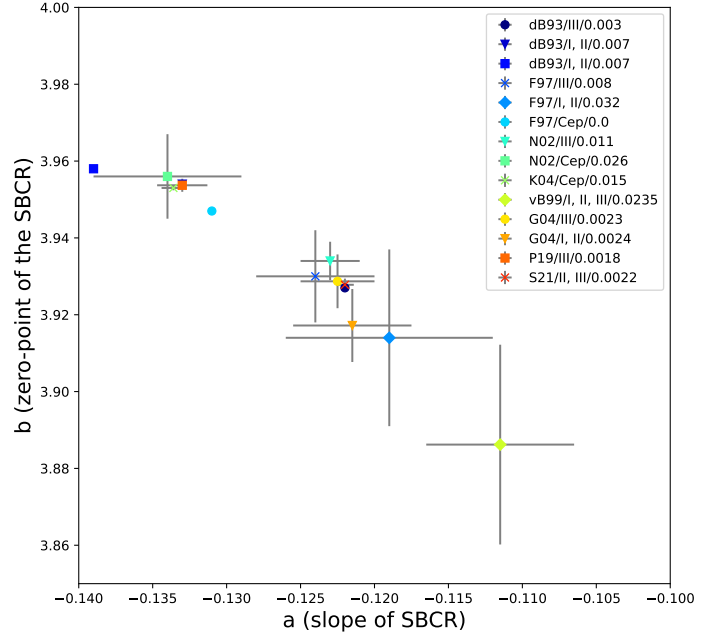


Fig. 7. Comparison of the slope and zero point of the linear SBCR in the literature.

In order to derive the angular diameter curve, we considered the interpolated curves in the V and K bands presented in Sect. 3. For the extinction, we used the value from the *Stilism*² online tool (Lallement et al. 2014; Capitanio et al. 2017) to compute the color excess $E(B - V)$. This tool produces tridimensional maps of the local interstellar matter (ISM). According to this map, the extinction is constant in a certain distance range for η Aql. We find $E(B - V) = 0.152$ mag in the case of η Aql. Using $R_V = 3.1$ which corresponds to the typical value in the diffuse ISM (Cardelli et al. 1989), we find $A_V = 0.47$ mag and $A_K = 0.089 \times A_V = 0.04$ mag, according to Nishiyama et al. (2009). We arbitrarily set a conservative uncertainty on A_V of 0.1 mag. Following Salsi et al. (2020a), the uncertainty on A_K was neglected. The angular diameter values were calculated using Eq. (5). Associated with these values, we considered the two following uncertainties (Salsi et al. 2020a,b). The first uncertainty is that on the limb-darkened angular diameter due to the uncertainty on the coefficients of the SBCR,

$$\sigma_{\theta_{\text{LD,coo}}} = 2 \ln(10) \theta_{\text{LD}} \left\{ [(V - K) - 0.881A_V]^2 \sigma_a^2 + \sigma_b^2 \right\}^{1/2}. \quad (9)$$

The second uncertainty is that on the limb-darkened angular diameter that is due to the photometric uncertainties on V , K , and A_V ,

$$\sigma_{\theta_{\text{LD,pho}}} = 2 \ln(10) \theta_{\text{LD}} \left\{ a^2 (\sigma_V^2 + \sigma_K^2 + 0.014\sigma_{A_V}^2) \right\}^{1/2}. \quad (10)$$

In Fig. 8 we plot the angular diameter curves obtained with the 19 SBCRs from Tables 2 and 3. The dark gray zone corresponds to the uncertainty on the coefficients of the SBCR of K04. As a comparison, we overplot the limb-darkened angular diameter derived from interferometry with VINCI/VLTI (Kervella et al. 2004c), PTI (Lane et al. 2002), and FLUOR/CHARA (Mérand et al. 2015). The VINCI/VLTI angular diameters are found to be larger (and have larger uncertainties) than the PTI and FLUOR/CHARA measurements, which

² The online tool is available at <http://stilism.obspm.fr>

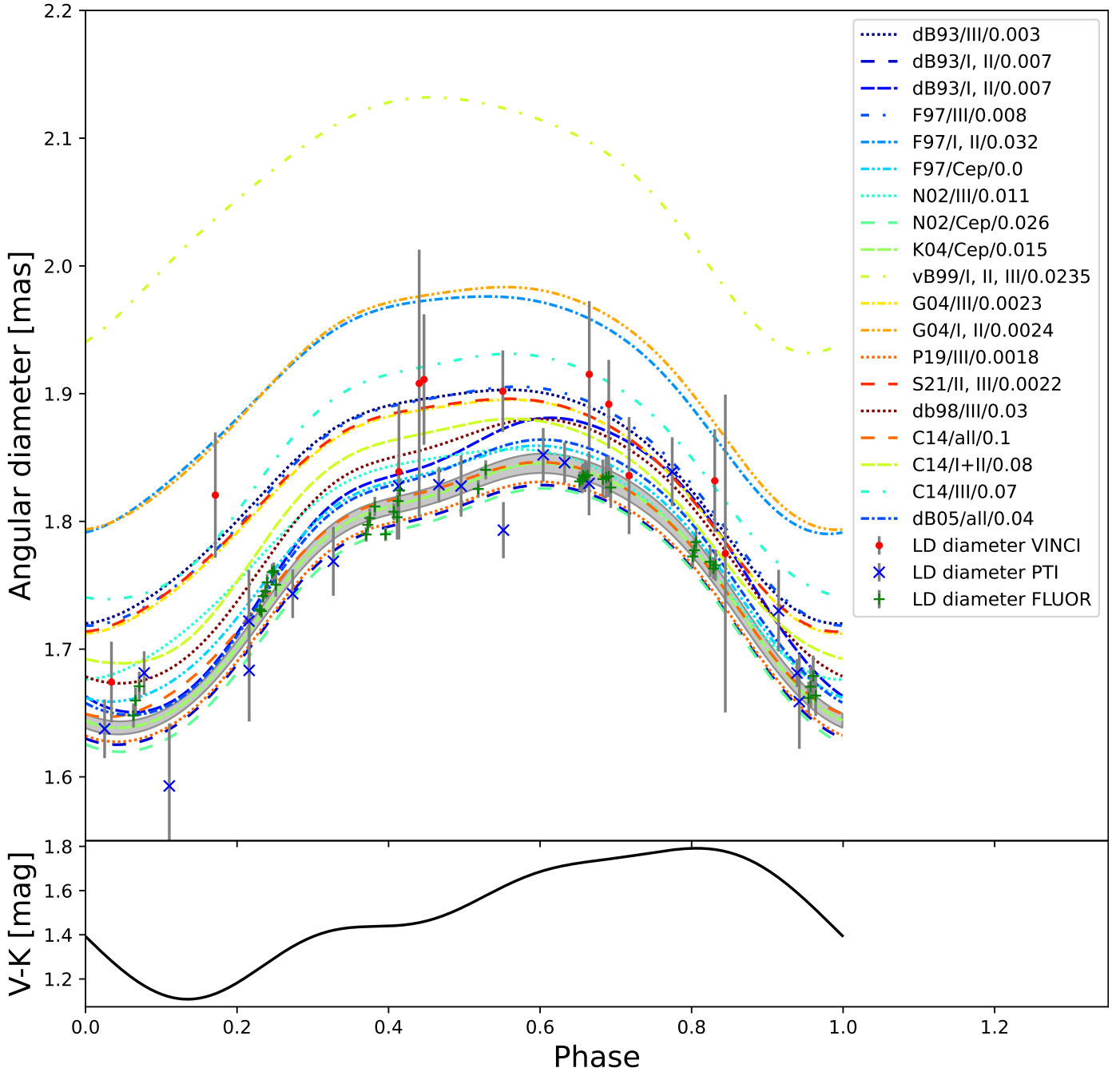


Fig. 8. Angular diameter curves as derived from SBCRs. Top: angular diameter of η Aql as a function of the pulsation phase for different SBCRs (from Fig. 6) combined with the V and K light curves (Fig. 5). The gray band corresponds to the uncertainty on the angular diameters caused by the uncertainty of the coefficients of the K04 SBCR. For comparison, we also plot the limb-darkened angular diameter as obtained by VINCI, PTI, and FLUOR measurements. Bottom: $V - K$ color of η Aql.

might be due simultaneously to a lack of data at high spatial frequencies and a bias due to a CSE at low spatial frequencies. In addition, most of the SBCRs fail to simultaneously reproduce the mean and the amplitude of the interferometric (PTI and FLUOR) angular diameter curves. We quantify the choice of the SBCR and the interferometric data set on the derived projection factor in Sect. 7.

6. Application of the inverse BW method

We derived the limb-darkened angular diameters (Eq. (5)) together with the associated uncertainties (Eqs. (9) and (10))

at the specific phases of K band measurements (Fig. 5 bottom panel). The V measurements were interpolated at the corresponding phases.

To do this, we applied the χ^2 minimization,

$$\chi^2 = \sum_i \frac{(\theta_{\text{obs}}(\phi_i) - \theta_{\text{model}}(\phi_i))^2}{\sigma_{\text{obs}}(\phi_i)^2}, \quad (11)$$

where $\theta_{\text{obs}}(\phi_i)$ are the limb-darkened angular diameters derived either from interferometry or from the different SBCRs (Eq. (5)). Here, ϕ_i is the pulsation phase corresponding to the i th measurement; $\sigma_{\text{obs}}(\phi_i)$ are the statistical uncertainties corresponding

to interferometric measurements or the uncertainties associated with the SBCR as defined in Eqs. (9) and (10). In the following, we consider either one of these uncertainties or the quadratic sum of all of them depending on the purpose; $\theta_{\text{model}}(\phi_i)$ are the modeled limb-darkened angular diameters, defined as

$$\theta_{\text{model}}(\phi_i) = \bar{\theta} + 9.3009 p \pi \int \text{RV}(\phi_i) d\phi_i [\text{mas}], \quad (12)$$

where the conversion factor 9.3009 was defined using the solar radius given in Prša et al. (2016). In the following, RV is the interpolated radial velocity curve: either $\text{RV}_{\text{cc-c}}$, $\text{RV}_{\text{cc-g}}$ or RV_{c} for the individual lines listed in Table 1. π is the parallax of the star. Recently, Benedict et al. (2022) reanalyzed the *Hubble* Space Telescope Fine Guidance Sensor (FGS) astrometry, together with reference star parallax and proper motion priors from *Gaia* EDR3 (Gaia Collaboration 2020), in order to search for the close companion of η Aql. In addition to the Cepheid, the η Aql system is probably composed of an F-type star at 0.66 arcsec (Evans et al. 2013; Gallenne et al. 2014) and a closer companion with a spectral type of B9.8V (Evans 1991). We considered their best parallax (their Table 13 with *Gaia* priors), $\pi = 3.71 \pm 0.07$ mas. As discussed in their paper, this value provides an absolute *K*-band magnitude consistent with the Leavitt law, and in our case, it provides realistic projection factors (otherwise lower than 1 when the values in their tables 11 or 12 are used, i.e., without *Gaia* priors). Similarly to Benedict et al. (2022), we do not find irregularities in our radial velocity measurements. This suggests either a nearly face-on orientation or a very long period for the closer companion. The relative precision of this parallax is about 2%. This linearly translates into a statistical uncertainty on the projection factor. The mean angular diameter $\bar{\theta}$ and the projection factor p were fit in order to minimize χ^2 . Interestingly, Fig. 8 shows that the angular diameter curves associated with the different SBCRs follow the shape of the $V - K$ color variation, but with a slight shift in phase. In the minimization process, a phase shift between the radial velocity and the angular diameter was considered. The phase shift providing the lowest reduced χ^2 was adopted.

Figure 9 shows an example fit in the case of the K04 SBCR and using $\text{RV}_{\text{cc-c}}$. The uncertainties on the limb-darkened angular diameter correspond to the uncertainties associated with the photometry (Eq. (10)). We find $\theta_0 = 1.776 \pm 0.003$ mas and $p = 1.40 \pm 0.06$, with a reduced χ^2 of 0.6. The phase shift for the radial velocity curve is $\phi_0 = -0.02$ (see Table 5). In the next section, we quantify the impact of the SBCRs, the method we used to derive the radial velocity, the extinction, and possibly the CSE, on the projection factor.

7. Analysis of the uncertainties associated with the BW projection factor

We investigated different aspects, listed below, that might impact the BW projection factor.

7.1. Uncertainty on the photometry

This is the first important aspect. If the uncertainties on the photometry are considered (Eq. (10)), they have a non-negligible impact on the projection factor. The mean uncertainty of measurements in the *V* and *K* band are 0.04 mag and 0.01 mag, respectively (Fig. 5). When an uncertainty on A_V of 0.1 mag is also included, this translates into a mean uncertainty on the

angular diameters of about 0.03 mas (Fig. 9), and finally, into a statistical uncertainty on the projection factor of 0.06 in the case of the K04 SBCR, that is, about 4% (see Table 5).

7.2. Choice of the SBCR

In the literature, the SBCRs have been calibrated using different samples of stars and interferometric instruments, which explains the significant difference obtained in Fig. 6. The choice of the SBCR used to apply the inverse BW method is thus critical. We applied the inverse BW method (see previous section) for the different SBCRs of Tables 2 and 3 in order to derive the mean angular diameter and the projection factor. This was also done using interferometric measurements obtained with VINCI, PTI, and FLUOR. In Fig. 10 we plot the derived projection factors as a function of the mean angular diameter θ_0 . The uncertainties associated with the measurements correspond to Eq. (10), that is, the photometric uncertainties. The green cross with an error bar in red corresponds to the case of K04, which is our reference. In the second panel, we provide the reduced χ^2 , and the third panel shows the phase shift of the best fit. The results are listed in Table 5. The values of the projection factor range from 1.23 (N02 III) to 1.70 (vB99 I, II, III) with a statistical dispersion of 0.11 on the projection factor (or 8%). The rms is an indicator of the robustness of the relations. When we exclude F97 (Cep), which provides no rms, the rms of SBCRs in Tables 2 and 3 ranges (using the F_V definition) from 0.0018 mag (P19) to 0.032 (F97 I, II) with a mean of 0.01 mag. The 5 SBCRs with the lowest rms are dB93 (III), G04 (III), G04 (I, II), P19 (III), and S21 (II, III) with 0.0030, 0.0023, 0.0024, 0.0018, and 0.0022 mag, respectively. The $V - K$ validity domain of none of these relations is consistent with the color range of η Aql, except for G04 (I, II; see Table 2). The K04 relation that is often used in the literature for the BW application has an rms of 0.015 mag, which is larger by an order of magnitude. The corresponding projection factors associated with these relations are 1.24 ± 0.04 , 1.25 ± 0.17 , 1.29 ± 0.25 , 1.37 ± 0.08 , and 1.24 ± 0.06 , respectively. In addition, when we consider the FLUOR/CHARA interferometric measurements, which have the best quality in term of precision and phase coverage, we find a projection factor of 1.23 ± 0.03 . The upper panel of Fig. 8 shows that the K04 SBCRs provide an excellent agreement at maximum radius, but not at minimum radius (see phase 0.05), which leads to an overestimation of the amplitude of the angular diameter (compared to FLUOR) and thus to a larger projection factor of 1.40 ± 0.06 . This is the same for P19 (III; see Fig. 8 and also Fig. 10). We finally have four SBCRs whose rms is lower than 0.03 mag and that provide consistent projection factors (1.24–1.29) that are also consistent with the projection factor derived from the best available interferometric data (FLUOR/CHARA, $p = 1.23$). This analysis suggests that the projection factor of η Aql is most probably about 1.25. For the summary plot at the end of this section, we used the recent SBCR of S21 (II, III).

7.3. Uncertainties on the coefficients of the SBCR

The statistical dispersion on the projection factor that is due to the uncertainty on the coefficients (Eq. (9)) of the K04 SBCR is 0.02 (or 1.5%) when the K04 SBCR (Table 5) is considered.

7.4. Method for deriving the radial velocity

As indicated in Sect. 6, when we consider the K04 SBCR and the $\text{RV}_{\text{cc-c}}$ radial velocity (see Sect. 2), we obtain $p = 1.40 \pm 0.06$.

Table 5. Results of the inverse BW method when it was applied to different SBCRs (Cols. 1 and 2).

Ref	Class	ϕ_0	χ_{red}	θ_0	σ_{θ_0}	p	$\sigma_{p_{\text{coe}}}$	$\sigma_{p_{\text{pho}}}$	$\sigma_{p_{\text{tot}}}$
dB93*	III	+0.02	1.0	1.847	0.002	1.24	0.00	0.04	0.04
dB93	I, II	-0.02	0.5	1.761	0.003	1.37	0.00	0.06	0.06
dB93	I, II	-0.03	0.4	1.803	0.004	1.54	0.00	0.07	0.07
F97 ⁺	III	+0.02	0.9	1.847	0.002	1.27	0.29	0.04	0.29
F97	I, II	+0.04	1.1	1.920	0.002	1.26	0.57	0.04	0.57
F97	Cep	-0.01	0.6	1.793	0.003	1.36	0.00	0.05	0.05
N02	III	+0.02	0.9	1.801	0.002	1.23	0.12	0.04	0.13
N02	Cep	-0.02	0.5	1.757	0.003	1.39	0.26	0.06	0.27
K04	Cep	-0.02	0.5	1.776	0.003	1.40	0.02	0.06	0.06
vB99	Var	+0.08	1.3	2.684	0.002	1.69	1.94	0.04	1.95
vB99 ⁺	I, II, III	+0.07	1.3	2.072	0.002	1.31	0.67	0.03	0.67
G04*	III	+0.02	0.9	1.839	0.002	1.25	0.17	0.04	0.17
G04	I, II	+0.03	1.0	1.926	0.002	1.29	0.25	0.04	0.25
P19 ⁺	III	-0.02	0.5	1.763	0.003	1.37	0.05	0.06	0.08
S21 ⁺	II, III	+0.02	1.0	1.840	0.002	1.24	0.04	0.04	0.06
db98*	III	-0.01	0.1	1.791	0.001	1.39	0.01		
C14	all	-0.01	0.0	1.761	0.003	1.33	0.05		
C14	I+II	+0.00	0.0	1.797	0.002	1.32	0.04		
C14	III	+0.01	0.0	1.848	0.002	1.33	0.04		
dB05	all	-0.02	0.1	1.771	0.001	1.44	0.02		
VINCI		+0.01	0.3	1.819	0.014	1.42			0.24
PTI		-0.02	1.0	1.762	0.005	1.28			0.09
FLUOR		-0.01	1.2	1.759	0.001	1.23			0.03

mas mas

Notes. The phase shift ϕ_0 and the χ_{red} are provided together with the results of the fit, i.e., the mean angular diameter θ_0 and the projection factor p . The uncertainty on the projection factor is decomposed into uncertainties due to the uncertainty on the coefficients of the SBCR ($\sigma_{p_{\text{coe}}}$, Eq. (9)) and to the uncertainty on the photometry ($\sigma_{p_{\text{pho}}}$, Eq. (10)). $\sigma_{p_{\text{tot}}}$ is the quadratic sum of these uncertainties. For the nonlinear SBCRs of Table 3, only $\sigma_{p_{\text{coe}}}$ is provided. For interferometric results, i.e., VINCI (Kervella et al. 2004c), PTI (Lane et al. 2002), and FLUOR (Mérand et al. 2015), only the total uncertainty on the projection factor due to the uncertainty on the angular diameter measurements is provided. In the first column, the plus and asterisk indicate that the $V - K$ range of η Aql is not consistent or partially consistent, respectively, with the validity domain of the SBCR.

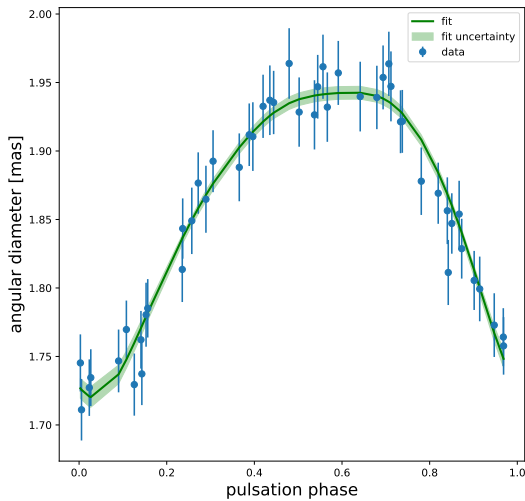


Fig. 9. Example of the fit when the inverse BW method was applied, using the K04 SBCR together with the V - and K -band photometry of Fig. 5. The derived angular diameters are plotted as a function of the pulsation phase together with the uncertainties propagated from the uncertainties on the V and K photometries. The best fit is indicated by the green line.

When we instead use $RV_{\text{cc-g}}$, as is usually done in the literature, we obtain $p = 1.33 \pm 0.06$, which is a non-negligible difference of 5%. This is also shown in Fig. 2, which shows that the amplitude of the $RV_{\text{cc-g}}$ is larger than the amplitude of the

$RV_{\text{cc-c}}$ curve. As already discussed in Nardetto et al. (2006), the projection factor cannot be separated from the method that is used to derive the radial velocity. The impact of the choice of the spectral line can also be considered, instead of using thousands of lines, as in the cc method. In the 17 spectral lines of Table 1, the projection factors range from 1.33 to 1.46 (with a standard deviation of 0.03). These values correspond to a range on the projection factor of 9%. These results are consistent with Nardetto et al. (2007).

7.5. Zero point of the SBCR

In Fig. 11a we quantify the impact of the zero point of the SBCR on the mean angular diameter and on the projection factor. To do this, we applied the inverse BW method and again considered the K04 SBCR as a reference ($p = 1.40$). We considered only the statistical uncertainties associated with the photometry in the fit. The zero point of the SBCR was set to values between -0.1 (compared to the zero point of the K04 SBCR) and 0.1 , with steps of 0.01 , which corresponds to the typical uncertainty on the zero point of SBCRs in Table 2. The resulting mean angular diameters, projection factors, and reduced χ^2 are plotted as a function of the zero point offset. We find that an offset of -0.01 mag ($+0.01$ mag) on the zero point of the SBCR increases (decreases) the projection factor to $p = 1.47$ ($p = 1.33$), which corresponds to $\pm 5\%$.

Table 4 shows that the SBCRs are based on various photometric systems, in particular in the infrared domain. An offset

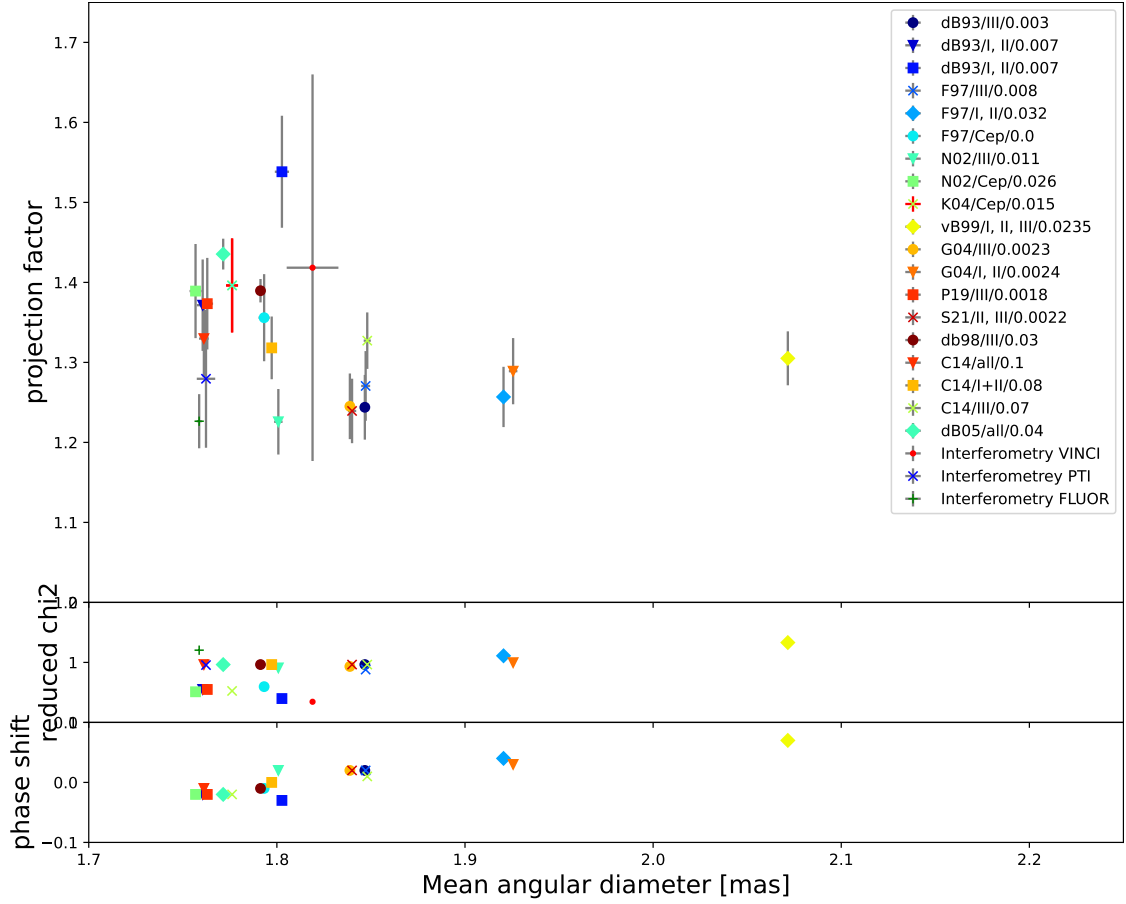


Fig. 10. Top: dependence of the calculated projection factors on the mean angular diameters from our analysis (from Table 5) when the stellar parallax from Benedict et al. (2022) was adopted. Values calculated using both the different SBCRs and the interferometric angular diameter curves are presented. Middle: reduced χ^2 plotted as a function of the mean angular diameter. Bottom: phase shift plotted as a function of mean angular diameter.

in photometry (in the visual and/or in the infrared) translates into an offset on the zero point of the SBCR, which is typically an order of magnitude lower in magnitude. Conversion relations between the various systems indicated in Table 4 in the literature (see for instance Fouque & Gieren 1997; Groenewegen et al. 2004; Glass 1985) show that the offsets between the magnitudes are typically about 0.01 mag. This translates into an offset on the zero point of the SBCR of typically 0.001 mag, which corresponds to an offset on the projection factor of 0.5%. Interestingly, the offset between the K -band magnitudes (regardless of the system considered) and the 2MASS system is larger, typically 0.044 magnitude (Bessell 2005), which corresponds to an offset on the zero point of the SBCR of about 0.005 mag (see Table 5 of Salsi et al. 2021) and finally to a non-negligible effect on the projection factor of about 2.5%.

7.6. Slope of the SBCR

With the same method as for the zero point, we quantified the impact of the slope of the SBCR. We thus considered different slopes from -0.06 to 0.06 with steps of 0.002 (which is the typical uncertainty on the slope of SBCR in Table 2), and we plot the resulting mean angular diameter, projection factor, and reduced χ^2 in Fig. 11b. We find that a difference -0.002 (0.002) on the slope of the SBCR increases (decreases) the projection factor to 1.46 (1.33). Interestingly, the reduced χ^2 is highly sensitive to the slope of the SBCR. This suggests that the slope of the SBCR is

critical for reproducing the shape to the angular diameter curve, that is, a shape that is consistent with the shape derived from the integrated radial velocity curve. It also shows that the projection factor is sensitive to the nonlinearity of the SBCRs listed in Table 3.

7.7. $E(B-V)$ value

In Fig. 11c we show the impact of the $E(B-V)$ value on the projection factor. In our reference fit (K04 SBCR), the $E(B-V)$ value was 0.152 (see Sect. 5). For our test, we set $E(B-V)$ from 0 to 0.8 mag (with steps of 0.05). When we consider $E(B-V) = 0.1$ ($E(B-V) = 0.2$), we find $p = 1.42$ ($p = 1.38$). This means that basically, an increase of 0.1 in $E(B-V)$ translates into a decrease in the projection factor of 3% . This is small because we used the $V-K$ color.

7.8. Impact of the CSE in the visible domain

In the SPIPS analysis (Mérand et al. 2005; Trahin et al. 2021), an ad hoc infrared excess law is necessary to fit the atmosphere models. This infrared excess is physically understood by the presence of a CSE, whose physical nature is still under analysis (Hocdé et al. 2021). It is also not excluded that the CSE emits some light in the visible domain (Nardetto et al. 2016) or even absorbs it (Hocdé et al. 2020b). Thus, if a CSE like this exists, it might bias the visible magnitude (positively or negatively),

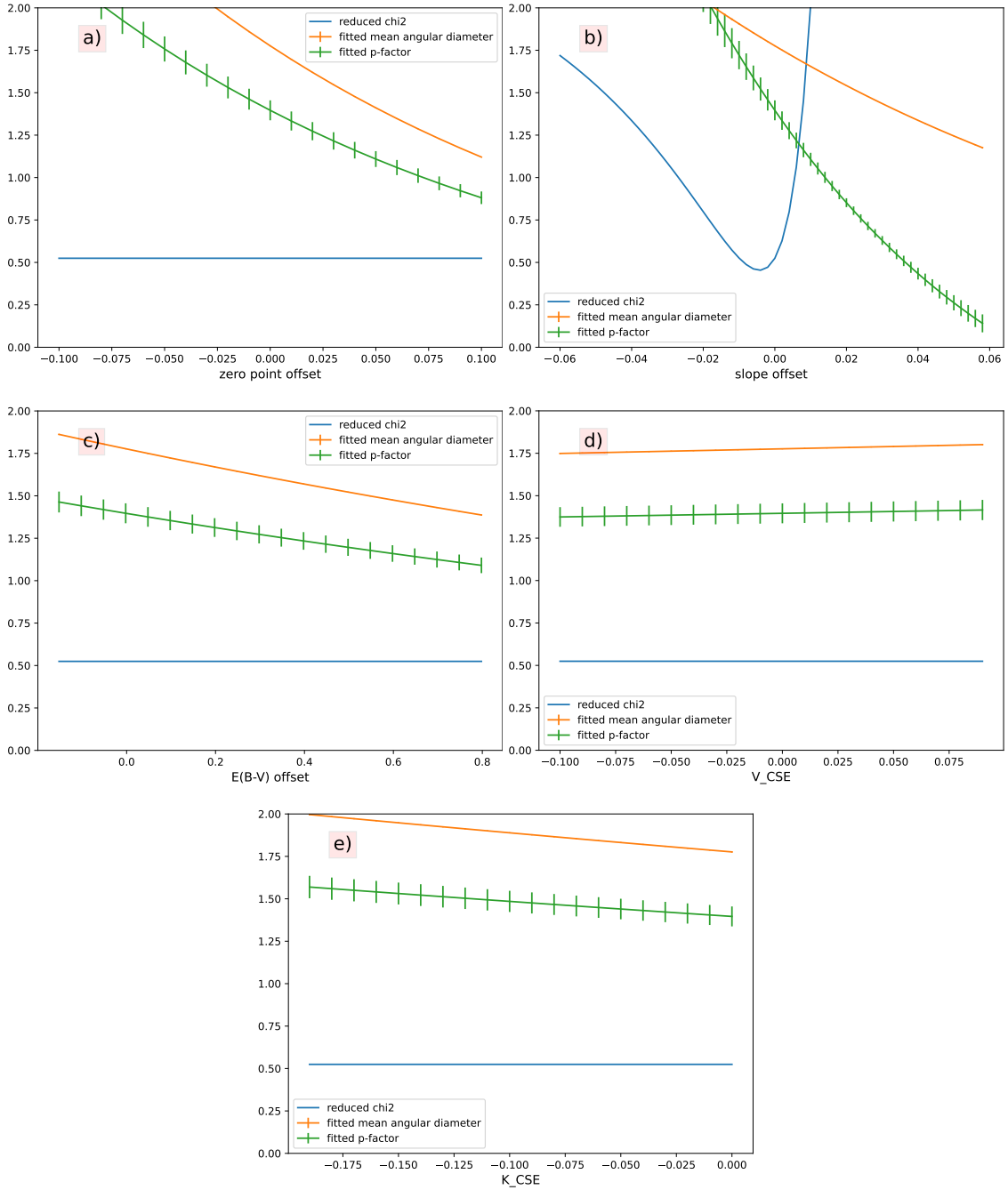


Fig. 11. Application of the inverse BW method to η Aql using the K04 SBCR. The derived mean angular diameter, the projection factor and the reduced χ^2 are shown when varying different parameters: (a) the zero point of the SBCR, (b) the slope of the SBCR, (c) the $E(B - V)$, value (d) considering an offset on the V magnitude due to a CSE, (e) considering an offset on the K magnitude due to a CSE.

which we can parameterize in Eqs. (5) and (6) by replacing V by $V + V_{\text{cse}}$. If the observed magnitude V_{\star} is replaced by $V_{\star} + V_{\text{cse}}$ with V_{cse} positive (negative), the $V_{\star} + V_{\text{cse}}$ magnitude is larger (smaller), which corresponds to a fainter (brighter) observed object (star + CSE) because the CSE is absorbing (emitting) light. We also recall that an offset in magnitude for the CSE corresponds to a flux that is a constant fraction of the flux of the star. We considered V_{cse} from -0.1 to 0.1 magnitudes (with steps of 0.01), and we plot the derived mean angular diameter, projection factor, and reduced χ^2 in Fig. 11d. We find that $V_{\text{cse}} = -0.1$ ($V_{\text{cse}} = +0.1$) reduces (increases) the projection factor from $p = 1.40$ to $p = 1.38$ ($p = 1.42$). The effect of the CSE in the visible domain is rather small, about 1.5% . However,

this is a first-order analysis as the CSE can also involve phase-dependent mechanisms that could alter the amplitude of the V and K magnitudes. Moreover, absorption in the visible comes very likely with re-emission in the infrared, so that the impacts of CSE in the visible and in the infrared are correlated. Dedicated models are necessary to study the impact of these effects on the projection factor in detail.

7.9. Impact of the CSE in the infrared domain

We repeated the analysis in the infrared domain. We thus replaced K by $K + K_{\text{cse}}$ in Eqs. (5) and (6). However, we considered only negative values for K_{cse} (CSE emitting light)

because so far, only infrared excess was observed in Cepheids, either in the spectral energy distributions (Trahin et al. 2021; Gallenne et al. 2021; Groenewegen 2020) or by interferometry (Mérand et al. 2006, 2007). However, we recall that a compact envelope of ionized gas can also potentially generate absorption in the K band (Hocdé et al. 2020b, their Fig. 10), but this needs to be investigated further. In this work, we thus considered K_{cse} values from 0.0 to -0.2 mag with steps of 0.01 (Fig. 11e). We find that $K_{\text{cse}} = -0.1$ mag corresponds to an increase in the projection factor from $p = 1.40$ to $p = 1.49$ (about 6%), which is clearly not negligible.

The nine uncertainty sources we discussed in this section are represented in the summary Fig. 12. In this figure, the uncertainties on the projection factor and the mean angular diameter of η Aql are provided in different cases (shifted by $n * 0.5$ mas for clarity, where n is an integer). Following our discussion about the choice of the SBCR (Sect. 7.2), we applied the inverse BW method to η Aql using the S21 SBCR instead of K04. We considered the $RV_{\text{cc-c}}$ definition of the velocity, the Benedict et al. (2022) parallax, and $E(B - V) = 0.152$ mag (see Sects. 5 and 6 for details). The resulting projection factor is 1.24 and $\theta_0 = 1.84$ mas (red cross in the figure). The different blue bars correspond to different cases, as indicated in the figure caption.

8. Conclusion

The projection factor of η Aql clearly depends on the method that is used when the inverse BW method is applied: interferometry, SBCR, or even a combination of both (SPIPS). The choice of the SBCR is particularly crucial, as is the method that is used to derive the radial velocity curve: $RV_{\text{cc-g}}$, $RV_{\text{cc-c}}$ or even single-line analysis (RV_c). In addition to this, the projection factor might be biased by the calculation of extinction and by the presence or absence of a CSE. This CSE can indeed create an offset in the visible magnitude, in the infrared, or even in both. In addition, the statistical precision that can be expected on the projection is closely linked to the precision of the photometry, the precision on the coefficients of the SBCR, and also to the precision of the stellar parallax.

Five SBCRs are suitable for Cepheids in the literature with an rms lower than 0.003 mag (using the F_V definition). Four of these five relations are consistent with each other within the $V - K$ validity domain of η Aql. These four SBCRs also provide amplitudes of the angular diameter curve that are consistent with the best interferometric observations to date (FLUOR). However, offsets in terms of mean angular diameters (typically 0.1–0.2 mas) are found between the angular diameter curves from these SBCRs and the interferometric one. Thus, when these four SBCRs are considered together with the $RV_{\text{cc-c}}$ definition of the radial velocity, we find $p = 1.24 \pm 0.04$ (dB93 III), $p = 1.25 \pm 0.17$ (G04 III), $p = 1.29 \pm 0.25$ (G04 I and II), and $p = 1.24 \pm 0.06$ (S21 II and III), and $p = 1.23 \pm 0.03$ when FLUOR interferometric measurements are considered. Including a 2% statistical precision due to the uncertainty on the parallax (Benedict et al. 2022) does not change the global uncertainties on these projection factor. Thus, evidence indicates a projection factor for η Aql of about 1.25, which agrees with hydrodynamical models (Nardetto et al. 2004) and projection factors from eclipsing binaries (Pilecki et al. 2013) for short-period Cepheids. Nevertheless, additional studies are necessary to confirm this result. In particular, the disagreements between SBCRs in the literature need clarification, even if their origin is probably due to the use of different stellar samples, methods, and instruments.

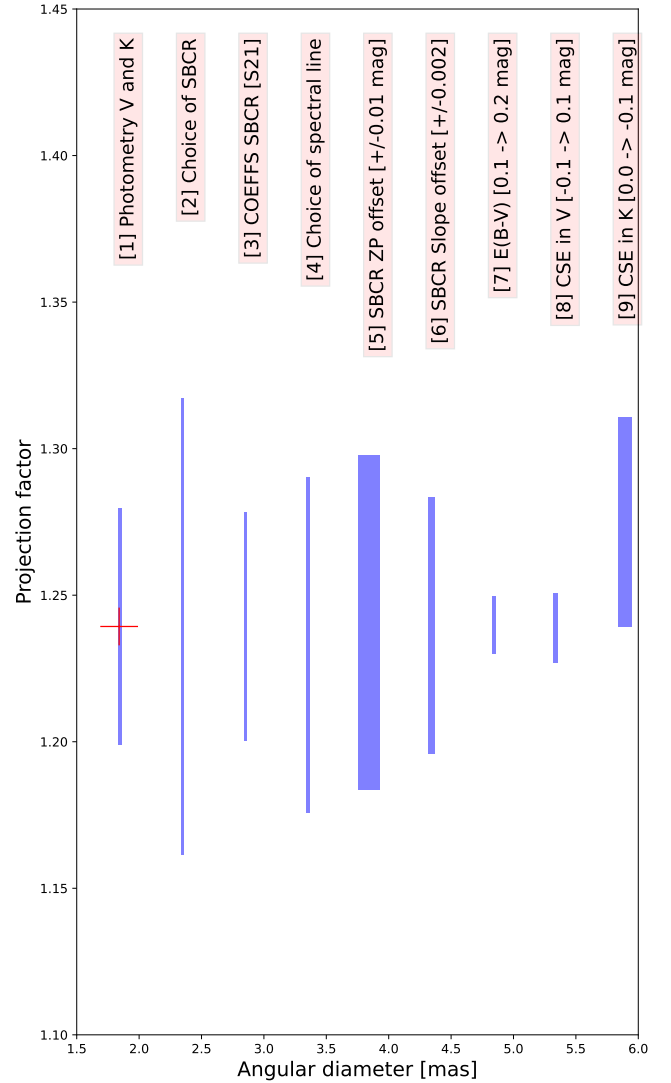


Fig. 12. Different sources of statistical and systematical uncertainties that can affect the projection factor of Cepheids. (1) Statistical uncertainty on the projection due to the uncertainty on the photometry (V , K , and A_V ; blue bar). The resulting uncertainty on θ_0 is negligible (lower than the thickness of the bar). The red cross is the reference (see the text). (2) Same as panel 1, except that the value of θ_0 is shifted by 0.5 mas for clarity. The blue bar corresponds to the systematical uncertainty on p due to the choice of the SBCR in the literature, i.e., it corresponds to the standard deviation of p values in Fig. 10 or in Table 5. (3) Statistical uncertainties corresponding to the uncertainties on the coefficients of the S21 SBCR. (4) Range over which the projection factor varies (i.e., bias or systematics) depending on the choice of the spectral line in order to derive the radial velocity (among the list of 17 lines of Table 1). (5) Indicative systematical uncertainties on p and θ_0 due to a positive or negative 0.01 mag shift on the zero point of the SBCR. (6) Indicative systematical uncertainties on p and θ_0 due to a positive or negative 0.01 shift on the slope of the SBCR. (7) Offsets on p and θ_0 when $E(B - V)$ changes from 0.1 to 0.2 mag (instead of 0.152). (8) Offsets on p and θ_0 when a shift in V from -0.1 to 0.1 mag is considered (due to a possible CSE) instead of 0 in the original fit (item 1). (9) Offsets on p and θ_0 when a shift in K of -0.1 mag is considered (due to a possible CSE) instead of 0.

The impact of the CSE of Cepheids when calibrating and using the SBCRs needs clarification as well. In particular, the projection factors that we obtain (around 1.25) assume that η Aql has no CSE that could alter the visual and/or the K -band magnitudes. It is still unclear whether the CSE could bias the V and/or K -band

magnitudes, and if it does, by which amount. This is under investigation (Trahin et al. 2021; Hocdé et al. 2020b; Groenewegen 2020).

Thus, in order to compare the projection factor of Cepheids, a consistent method is required. First, a dedicated SBCR should be used that was calibrated using homogeneous photometric and interferometric measurements. The same photometric system should be used when the SBCR is applied. However, to use such an SBCR, it might be necessary to verify the consistency of the SBCR for various Cepheids with different periods and at all pulsation phases. The upcoming instrument CHARA/SPICA (Mourard et al. 2022) may help to improve the SBCR of Cepheids in the near future. Second, if possible, a single-line analysis (or a few lines) should be used instead of the cross-correlation approach. Importantly, the centroid method is strongly favored as it is independent of the rotation and the full width at half maximum of the line. Third, the CSE of Cepheids in the instability strip should be studied, characterized, and parameterized in the calibration or use of the SBCR. This can also be done in the SPIPS analysis. Fourth, it also seems important to secure homogeneous and precise photometric and spectroscopic data in order to improve the statistical precision on the projection. The community should achieve this in the coming years to understand the projection factor in depth, and thus to understand the physics of Cepheids.

Acknowledgements. The observations leading to these results have received funding from the European Commission's Seventh Framework Programme (FP7/2013-2016) under grant agreement number 312430 (OPTICON). The authors thank the GAPS observers F. Borsa, L. Di Fabrizio, R. Fares, A. Fiorenzano, P. Giacobbe, J. Maldonado, and G. Scandariato. The authors thank the CHARA Array, which is funded by the National Science Foundation through NSF grants AST-0606958 and AST-0908253 and by Georgia State University through the College of Arts and Sciences, as well as the W. M. Keck Foundation. This research has made use of the SIMBAD and VIZIER³ databases at CDS, Strasbourg (France), and of the electronic bibliography maintained by the NASA/ADS system. W.G. gratefully acknowledges financial support for this work from the BASAL Centro de Astrofísica y Tecnologías Afines (CATA) PFB-06/2007, and from the Millenium Institute of Astrophysics (MAS) of the Iniciativa Científica Milenio del Ministerio de Economía, Fomento y Turismo de Chile, project IC120009. W.G. also acknowledges support from the ANID BASAL project ACE210002. Support from the Polish National Science Center grant MAESTRO 2012/06/A/ST9/00269 and DIR/WK/2018/09 grants of the Polish Ministry of Science and Higher Education is also acknowledged. E.P. and M.R. acknowledge financial support from PRIN INAF-2014. The authors acknowledge the support of the French Agence Nationale de la Recherche (ANR), under grant ANR-15-CE31-0012-01 (project UnlockCepheids) and the financial support from "Programme National de Physique Stellaire" (PNPS) of CNRS/INSU, France. A.G. acknowledges support from the ANID-ALMA fund No. ASTRO20-0059. B.P. gratefully acknowledges support from the Polish National Science Center grant SONATA BIS 2020/38/E/ST9/00486. This work has made use of data from the European Space Agency (ESA) mission *Gaia*, processed by the *Gaia* Data Processing and Analysis Consortium (DPAC). Funding for the DPAC has been provided by national institutions, in particular the institutions participating in the *Gaia* Multilateral Agreement. The research leading to these results has received funding from the European Research Council (ERC) under the European Union's Horizon 2020 research and innovation program (projects CepBin, grant agreement 695099, and UniverScale, grant agreement 951549). V.H. is supported by the National Science Center, Poland, Sonata BIS project 2018/30/E/ST9/00598.

References

- Anderson, R. I. 2014, *A&A*, **566**, L10
 Anderson, R. I., Mérand, A., Kervella, P., et al. 2016, *MNRAS*, **455**, 4231
 Baade, W. 1926, *Astron. Nachr.*, **228**, 359
 Barnes, III, T. G., Fernley, J. A., Frueh, M. L., et al. 1997, *PASP*, **109**, 645
 Barnes, III, T. G., Storm, J., Jefferys, W. H., Gieren, W. P., & Fouqué, P. 2005, *ApJ*, **631**, 572
 Benedict, G. F., Barnes, T. G., Evans, N. R., et al. 2022, *AJ*, **163**, 282
 Berdnikov, L. N. 2008, *VizieR Online Data Catalog: II/285*
 Bessell, M. S. 2005, *ARA&A*, **43**, 293
 Borgniet, S., Kervella, P., Nardetto, N., et al. 2019, *A&A*, **631**, A37
 Capitanio, L., Lallement, R., Vergely, J. L., Elyajouri, M., & Monreal-Ibero, A. 2017, *A&A*, **606**, A65
 Cardelli, J. A., Clayton, G. C., & Mathis, J. S. 1989, *ApJ*, **345**, 245
 Carter, B. S. 1990, *MNRAS*, **242**, 1
 Challouf, M., Nardetto, N., Mourard, D., et al. 2014, *A&A*, **570**, A104
 Cosentino, R., Lovis, C., Pepe, F., et al. 2012, *SPIE Conf. Ser.*, **8446**, 1
 Csörnyei, G., Szabados, L., Molnár, L., et al. 2022, *MNRAS*, **511**, 2125
 di Benedetto, G. P. 1993, *A&A*, **270**, 315
 di Benedetto, G. P. 1998, *A&A*, **339**, 858
 Di Benedetto, G. P. 2005, *MNRAS*, **357**, 174
 Elias, J. H., Frogel, J. A., Matthews, K., & Neugebauer, G. 1982, *AJ*, **87**, 1029
 Evans, N. R. 1991, *ApJ*, **372**, 597
 Evans, N. E., Bond, H. E., Schaefer, G. H., et al. 2013, *AJ*, **146**, 93
 Fouque, P., & Gieren, W. P. 1997, *A&A*, **320**, 799
 Fouqué, P., Arriagada, P., Storm, J., et al. 2007, *A&A*, **476**, 73
 Freedman, W. L., Madore, B. F., Scowcroft, V., et al. 2012, *ApJ*, **758**, 24
 Gaia Collaboration 2020, *VizieR Online Data Catalog: I/350*
 Gallenne, A., Mérand, A., Kervella, P., et al. 2013, *A&A*, **558**, A140
 Gallenne, A., Kervella, P., Mérand, A., et al. 2014, *A&A*, **567**, A60
 Gallenne, A., Pietrzyński, G., Graczyk, D., et al. 2018, *A&A*, **616**, A68
 Gallenne, A., Mérand, A., Kervella, P., et al. 2021, *A&A*, **651**, A113
 Gent, M. R., Bergemann, M., Serenelli, A., et al. 2022, *A&A*, **658**, A147
 Gezari, D. Y., Schmitz, M., Pitts, P. S., & Mead, J. M. 1993, *NASA RP (Reference Publication)*, Greenbelt: NASA, Goddard Space Flight Center, 3rd ed.
 Gieren, W., Pietrzyński, G., Bresolin, F., et al. 2005, *The Messenger*, **121**, 23
 Glass, I. S. 1985, *Irish Astron. J.*, **17**, 1
 Graczyk, D., Pietrzyński, G., Thompson, I. B., et al. 2020, *ApJ*, **904**, 13
 Graczyk, D., Pietrzyński, G., Galan, C., et al. 2021, *A&A*, **649**, A109
 Groenewegen, M. A. T. 2004, *MNRAS*, **353**, 903
 Groenewegen, M. A. T. 2020, *A&A*, **635**, A33
 Groenewegen, M. A. T., Romaniello, M., Primas, F., & Mottini, M. 2004, *A&A*, **420**, 655
 Hertzprung, E. 1913, *Astron. Nachr.*, **196**, 201
 Hindsley, R., & Bell, R. A. 1986, *PASP*, **98**, 881
 Hocdé, V., Nardetto, N., Borgniet, S., et al. 2020a, *A&A*, **641**, A74
 Hocdé, V., Nardetto, N., Lagadec, E., et al. 2020b, *A&A*, **633**, A47
 Hocdé, V., Nardetto, N., Matter, A., et al. 2021, *A&A*, **651**, A92
 Hunter, A., Macgregor, A., Szabo, T., et al. 2012, *Source Code Biol. Med.*, **7**, 1
 Johnson, H. L., Mitchell, R. I., Iriarte, B., & Wisniewski, W. Z. 1966, *Commun. Lunar Planet. Lab.*, **4**, 99
 Kervella, P., Bersier, D., Mourard, D., et al. 2004a, *A&A*, **428**, 587
 Kervella, P., Fouqué, P., Storm, J., et al. 2004b, *ApJ*, **604**, L113
 Kervella, P., Nardetto, N., Bersier, D., Mourard, D., & Coudé du Foresto, V. 2004c, *A&A*, **416**, 941
 Kervella, P., Thévenin, F., Di Folco, E., & Ségransan, D. 2004d, *A&A*, **426**, 297
 Kervella, P., Mérand, A., Perrin, G., & Coudé du Foresto, V. 2006, *A&A*, **448**, 623
 Kiss, L. L. 1998, *ASP Conf. Ser.*, **135**, 173
 Lallement, R., Vergely, J. L., Valette, B., et al. 2014, *A&A*, **561**, A91
 Lane, B. F., Kuchner, M. J., Boden, A. F., Creech-Eakman, M., & Kulkarni, S. R. 2000, *Nature*, **407**, 485
 Lane, B. F., Creech-Eakman, M. J., & Nordgren, T. E. 2002, *ApJ*, **573**, 330
 Leavitt, H. S., & Pickering, E. C. 1912, *Harvard College Observ. Circ.*, **173**, 1
 Ligi, R., Creevey, O., Mourard, D., et al. 2016, *A&A*, **586**, A94
 Lindemann, F. A. 1918, *MNRAS*, **78**, 639
 Mérand, A., Kervella, P., Coudé du Foresto, V., et al. 2005, *A&A*, **438**, L9
 Mérand, A., Kervella, P., Coudé du Foresto, V., et al. 2006, *A&A*, **453**, 155
 Mérand, A., Aufdenberg, J. P., Kervella, P., et al. 2007, *ApJ*, **664**, 1093
 Mérand, A., Kervella, P., Breifelder, J., et al. 2015, *A&A*, **584**, A80
 Mermilliod, J. C., Mermilliod, M., & Hauck, B. 1997, *A&AS*, **124**, 349
 Moffett, T. J., & Barnes, III, T. G. 1984, *ApJS*, **55**, 389
 Mourard, D., Nardetto, N., ten Brummelaar, T., et al. 2018, *SPIE Conf. Ser.*, **10701**, 1070120
 Mourard, D., Berio, P., Pannetier, C., et al. 2022, *SPIE Conf. Ser.*, **12183**, 1218308
 Nardetto, N. 2018, *ArXiv e-prints [arXiv:1801.04158]*
 Nardetto, N., Fokin, A., Mourard, D., et al. 2004, *A&A*, **428**, 131
 Nardetto, N., Mourard, D., Kervella, P., et al. 2006, *A&A*, **453**, 309
 Nardetto, N., Mourard, D., Mathias, P., Fokin, A., & Gillet, D. 2007, *A&A*, **471**, 661
 Nardetto, N., Stoekl, A., Bersier, D., & Barnes, T. G. 2008, *A&A*, **489**, 1255

³ Available at <http://cdsweb.u-strasbg.fr/>

- Nardetto, N., Gieren, W., Kervella, P., et al. 2009, *A&A*, 502, 951
 Nardetto, N., Mathias, P., Fokin, A., et al. 2013, *A&A*, 553, A112
 Nardetto, N., Poretti, E., Rainer, M., et al. 2014, *A&A*, 561, A151
 Nardetto, N., Mérand, A., Mourard, D., et al. 2016, *A&A*, 593, A45
 Nardetto, N., Poretti, E., Rainer, M., et al. 2017, *A&A*, 597, A73
 Neugebauer, G., & Leighton, R. B. 1969, *Two-micron Sky Survey. A Preliminary Catalogue* (NASA SP, Washington: NASA)
 Ngeow, C.-C., Neilson, H. R., Nardetto, N., & Marengo, M. 2012, *A&A*, 543, A55
 Nishiyama, S., Tamura, M., Hatano, H., et al. 2009, *ApJ*, 696, 1407
 Nordgren, T. E., Lane, B. F., Hindsley, R. B., & Kervella, P. 2002, *AJ*, 123, 3380
 Pannetier, C., Mourard, D., Berio, P., et al. 2020, *SPIE Conf. Ser.*, 11446, 114460T
 Pietrzyński, G., Graczyk, D., Gieren, W., et al. 2013, *Nature*, 495, 76
 Pietrzyński, G., Graczyk, D., Gallenne, A., et al. 2019, *Nature*, 567, 200
 Pilecki, B., Graczyk, D., Pietrzyński, G., et al. 2013, *MNRAS*, 436, 953
 Prša, A., Harmanec, P., Torres, G., et al. 2016, *AJ*, 152, 41
 Riess, A. G., Macri, L., Casertano, S., et al. 2011, *ApJ*, 730, 119
 Riess, A. G., Macri, L. M., Hoffmann, S. L., et al. 2016, *ApJ*, 826, 56
 Salsi, A., Nardetto, N., Mourard, D., et al. 2020a, *A&A*, 640, A2
 Salsi, A., Nardetto, N., Mourard, D., et al. 2020b, *A&A*, 641, C3
 Salsi, A., Nardetto, N., Mourard, D., et al. 2021, *A&A*, 652, A26
 Salsi, A., Nardetto, N., Plez, B., & Mourard, D. 2022, *A&A*, 662, A120
 Storm, J., Gieren, W., Fouqué, P., et al. 2011a, *A&A*, 534, A94
 Storm, J., Gieren, W., Fouqué, P., et al. 2011b, *A&A*, 534, A95
 Szabados, L. 1977, *Commun. Konkoly Observ. Hungary*, 70, 1
 Trahin, B., Breuval, L., Kervella, P., et al. 2021, *A&A*, 656, A102
 van Belle, G. T. 1999, *PASP*, 111, 1515
 Welch, D. L., & Evans, N. R. 1984, *JRASC*, 78, 207
 Wesselink, A. J. 1946, *Bull. Astron. Inst. Netherlands*, 10, 91
-
- ¹ Université Côte d’Azur, Observatoire de la Côte d’Azur, CNRS, Laboratoire Lagrange, Bd de l’Observatoire, CS 34229, 06304 Nice Cedex 4, France
 e-mail: Nicolas.Nardetto@oca.eu
² Universidad de Concepción, Departamento de Astronomía, Casilla 160-C, Concepción, Chile
³ Millenium Institute of Astrophysics, Avenue Libertador Bernardo O’Higgins 340, Casa Central, Santiago, Chile
⁴ Leibniz Institute for Astrophysics, An der Sternwarte 16, 14482 Potsdam, Germany
⁵ Nicolaus Copernicus Astronomical Center, Polish Academy of Sciences, ul. Bartycka 18, PL-00-716 Warszawa, Poland
⁶ LESIA (UMR 8109), Observatoire de Paris, PSL, CNRS, UPMC, Univ. Paris-Diderot, 5 place Jules Janssen, 92195 Meudon, France
⁷ European Southern Observatory, Alonso de Córdova 3107, Casilla 19001, Santiago 19, Chile
⁸ Unidad Mixta Internacional Franco-Chilena de Astronomía (CNRS UMI 3386), Departamento de Astronomía, Universidad de Chile, Camino El Observatorio 1515, Las Condes, Santiago, Chile
⁹ INAF – Osservatorio Astronomico di Brera, Via E. Bianchi 46, 23807 Merate (LC), Italy

Appendix A: Cross-correlated radial velocity tables

Table A.1. HARPS-N RV_{cc-g} – g (F6 template) radial velocities of η Aql.

BJD	ϕ	RV _{cc-g}	$\sigma_{RV_{cc-g}}$	BJD	ϕ	RV _{cc-g}	$\sigma_{RV_{cc-g}}$
2457108.7601	0.589	-15.2019	0.0006	2457172.7213	0.501	-16.1754	0.0007
2457109.7545	0.727	-5.6266	0.0006	2457173.5244	0.613	-14.5359	0.0009
2457112.7071	0.139	-31.6954	0.0014	2457173.5264	0.613	-14.5281	0.0009
2457112.7421	0.143	-31.6830	0.0006	2457173.7199	0.640	-13.2138	0.0008
2457113.7377	0.282	-27.0033	0.0004	2457173.7212	0.640	-13.2045	0.0008
2457114.7387	0.422	-20.4370	0.0008	2457174.5091	0.750	-3.1508	0.0017
2457114.7425	0.422	-20.4143	0.0014	2457174.5122	0.750	-3.0957	0.0014
2457137.7424	0.627	-14.0235	0.0006	2457174.5881	0.761	-1.9746	0.0008
2457137.7460	0.627	-14.0025	0.0011	2457174.5912	0.761	-1.9304	0.0008
2457142.7262	0.321	-25.2060	0.0008	2457175.5492	0.895	8.7276	0.0018
2457143.7003	0.457	-18.4493	0.0007	2457175.5505	0.895	8.7335	0.0019
2457143.7013	0.457	-18.4394	0.0007	2457175.7155	0.918	8.4551	0.0012
2457144.7062	0.597	-14.9161	0.0009	2457175.7167	0.918	8.4455	0.0012
2457144.7072	0.597	-14.9119	0.0009	2457176.5409	0.033	-19.8876	0.0016
2457145.7086	0.737	-4.6713	0.0006	2457176.5422	0.033	-19.9350	0.0017
2457145.7099	0.737	-4.6544	0.0006	2457176.7191	0.058	-25.4257	0.0009
2457146.6917	0.874	7.8032	0.0013	2457176.7201	0.058	-25.4519	0.0010
2457146.6930	0.874	7.8130	0.0015	2457177.5233	0.170	-31.1503	0.0011
2457147.7245	0.018	-15.6986	0.0011	2457177.5242	0.170	-31.1459	0.0011
2457148.7015	0.154	-31.4050	0.0008	2457177.6044	0.181	-30.8769	0.0010
2457148.7025	0.154	-31.3978	0.0009	2457177.6054	0.181	-30.8731	0.0011
2457153.7377	0.856	6.8569	0.0015	2457178.5383	0.311	-25.5400	0.0010
2457153.7387	0.856	6.8702	0.0016	2457178.5398	0.311	-25.5330	0.0009
2457154.6528	0.983	-4.5716	0.0042	2457178.7135	0.336	-24.3724	0.0011
2457154.6548	0.983	-4.6670	0.0041	2457178.7146	0.336	-24.3631	0.0011
2457155.6393	0.121	-31.4154	0.0075	2457203.5423	0.795	1.6335	0.0009
2457156.7401	0.274	-27.4204	0.0018	2457203.5468	0.796	1.7043	0.0006
2457157.6888	0.406	-21.3496	0.0019	2457204.5028	0.929	7.8041	0.0018
2457157.6908	0.406	-21.3370	0.0021	2457204.5038	0.929	7.7895	0.0018
2457158.7308	0.551	-15.0527	0.0010	2457205.5538	0.075	-28.3115	0.0010
2457159.7412	0.692	-9.0430	0.0010	2457205.5548	0.076	-28.3322	0.0010
2457159.7422	0.692	-9.0269	0.0011	2457206.5012	0.207	-29.9243	0.0009
2457169.5437	0.058	-25.5432	0.0014	2457206.5022	0.208	-29.9202	0.0009
2457169.5447	0.058	-25.5688	0.0013	2457207.5407	0.352	-23.6536	0.0008
2457169.6200	0.069	-27.3812	0.0014	2457207.5417	0.352	-23.6476	0.0007
2457169.6210	0.069	-27.4017	0.0015	2457208.5677	0.495	-16.3139	0.0008
2457170.5647	0.200	-30.1823	0.0013	2457208.5687	0.495	-16.3042	0.0009
2457170.5655	0.200	-30.1788	0.0013	2457209.6511	0.646	-12.6662	0.0011
2457170.7115	0.221	-29.4770	0.0014	2457209.6521	0.646	-12.6586	0.0012
2457170.7121	0.221	-29.4755	0.0013	2457210.6167	0.781	0.1251	0.0013
2457170.7141	0.221	-29.4616	0.0012	2457210.6177	0.781	0.1348	0.0012
2457170.7149	0.221	-29.4542	0.0011	2457269.5627	0.994	-8.4791	0.0017
2457171.5293	0.335	-24.4193	0.0016	2457269.5637	0.994	-8.5256	0.0017
2457171.5317	0.335	-24.4048	0.0015	2457271.5496	0.271	-27.4435	0.0008
2457171.6082	0.346	-23.9309	0.0007	2457271.5506	0.271	-27.4338	0.0008
2457171.6103	0.346	-23.9160	0.0007	2457272.5884	0.416	-20.6674	0.0008
2457172.5913	0.483	-17.1094	0.0006	2457272.5893	0.416	-20.6576	0.0008
2457172.5930	0.483	-17.0983	0.0007	2457273.5519	0.550	-15.0334	0.0008
2457172.7199	0.500	-16.1830	0.0007	2457273.5529	0.550	-15.0359	0.0009
days		km s ⁻¹	km s ⁻¹	days		km s ⁻¹	km s ⁻¹

Table A.2. HARPS-N RV_{cc-c} (F6 template) radial velocities of η Aql.

BJD	ϕ	RV _{cc-c}	$\sigma_{RV_{cc-c}}$	BJD	ϕ	RV _{cc-c}	$\sigma_{RV_{cc-c}}$
2457108.7601	0.589	-15.3761	0.0006	2457172.7213	0.501	-16.4848	0.0007
2457109.7545	0.727	-6.3331	0.0006	2457173.5244	0.613	-14.7596	0.0009
2457112.7071	0.139	-30.9229	0.0014	2457173.5264	0.613	-14.7451	0.0009
2457112.7421	0.143	-30.9397	0.0006	2457173.7199	0.640	-13.4911	0.0008
2457113.7377	0.282	-25.8473	0.0004	2457173.7212	0.640	-13.4843	0.0008
2457114.7387	0.422	-20.4125	0.0008	2457174.5091	0.750	-4.0068	0.0017
2457114.7425	0.422	-20.3984	0.0014	2457174.5122	0.750	-3.9731	0.0014
2457137.7424	0.627	-14.2505	0.0006	2457174.5881	0.761	-2.9180	0.0008
2457137.7460	0.627	-14.2298	0.0011	2457174.5912	0.761	-2.9023	0.0008
2457142.7262	0.321	-24.7608	0.0008	2457175.5492	0.895	7.4015	0.0018
2457143.7003	0.457	-18.6297	0.0007	2457175.5505	0.895	7.4186	0.0019
2457143.7013	0.457	-18.5950	0.0007	2457175.7155	0.918	7.2674	0.0012
2457144.7062	0.597	-15.1453	0.0009	2457175.7167	0.918	7.2925	0.0012
2457144.7072	0.597	-15.1173	0.0009	2457176.5409	0.033	-19.8247	0.0016
2457145.7086	0.737	-5.4541	0.0006	2457176.5422	0.033	-19.8756	0.0017
2457145.7099	0.737	-5.4392	0.0006	2457176.7191	0.058	-25.0661	0.0009
2457146.6917	0.874	6.5466	0.0013	2457176.7201	0.058	-25.0954	0.0010
2457146.6930	0.874	6.5514	0.0015	2457177.5233	0.170	-30.5110	0.0011
2457147.7245	0.018	-15.8904	0.0011	2457177.5242	0.170	-30.5049	0.0011
2457148.7015	0.154	-30.6799	0.0008	2457177.6044	0.181	-30.2474	0.0010
2457148.7025	0.154	-30.6725	0.0009	2457177.6054	0.181	-30.2386	0.0011
2457153.7377	0.856	5.5143	0.0015	2457178.5383	0.311	-25.1140	0.0010
2457153.7387	0.856	5.5248	0.0016	2457178.5398	0.311	-25.1088	0.0009
2457154.6528	0.983	-4.9432	0.0042	2457178.7135	0.336	-24.0095	0.0011
2457154.6548	0.983	-5.0159	0.0041	2457178.7146	0.336	-24.0044	0.0011
2457155.6393	0.121	-30.7510	0.0075	2457203.5423	0.795	0.5924	0.0009
2457156.7401	0.274	-26.8474	0.0018	2457203.5468	0.796	0.6528	0.0006
2457157.6888	0.406	-21.1738	0.0019	2457204.5028	0.929	6.8420	0.0018
2457157.6908	0.406	-21.1627	0.0021	2457204.5038	0.929	6.8340	0.0018
2457158.7308	0.551	-15.3880	0.0010	2457205.5538	0.075	-27.7975	0.0010
2457159.7412	0.692	-9.5467	0.0010	2457205.5548	0.076	-27.8137	0.0010
2457159.7422	0.692	-9.5392	0.0011	2457206.5012	0.207	-29.3577	0.0009
2457169.5437	0.058	-25.1674	0.0014	2457206.5022	0.208	-29.3583	0.0009
2457169.5447	0.058	-25.1881	0.0013	2457207.5407	0.352	-23.2804	0.0008
2457169.6200	0.069	-26.8909	0.0014	2457207.5417	0.352	-23.2737	0.0007
2457169.6210	0.069	-26.8949	0.0015	2457208.5677	0.495	-16.5356	0.0008
2457170.5647	0.200	-29.5809	0.0013	2457208.5687	0.495	-16.5355	0.0009
2457170.5655	0.200	-29.5861	0.0013	2457209.6511	0.646	-12.9839	0.0011
2457170.7115	0.221	-28.9194	0.0014	2457209.6521	0.646	-12.9836	0.0012
2457170.7121	0.221	-28.9326	0.0013	2457210.6167	0.781	-0.8593	0.0013
2457170.7141	0.221	-28.9101	0.0012	2457210.6177	0.781	-0.8316	0.0012
2457170.7149	0.221	-28.8955	0.0011	2457269.5627	0.994	-8.6815	0.0017
2457171.5293	0.335	-24.0206	0.0016	2457269.5637	0.994	-8.7346	0.0017
2457171.5317	0.335	-24.0052	0.0015	2457271.5496	0.271	-26.7610	0.0008
2457171.6082	0.346	-23.5647	0.0007	2457271.5506	0.271	-26.7476	0.0008
2457171.6103	0.346	-23.5457	0.0007	2457272.5884	0.416	-20.4835	0.0008
2457172.5913	0.483	-17.3346	0.0006	2457272.5893	0.416	-20.4687	0.0008
2457172.5930	0.483	-17.3298	0.0007	2457273.5519	0.550	-15.2903	0.0008
2457172.7199	0.500	-16.4919	0.0007	2457273.5529	0.550	-15.2798	0.0009
days		km s ⁻¹	km s ⁻¹	days		km s ⁻¹	km s ⁻¹